Finite Element Analysis of Shape Memory Alloy based members Undergoing Torsion

Thesis report submitted
for the fulfillment of the requirements
for the degree of
Master of Technology

by

Yash Kumar
(214103437)

Under the Supervision of

Dr. Atanu Banerjee
Associate Professor, IIT Guwahati

Department of Mechanical Engineering
Indian Institute of Technology Guwahati
Guwahati-781 039
June 2023

Certificate

This is to certify that the thesis work entitled "**Finite element analysis of Shape Memory Alloy based members undergoing torsion**", by Yash Kumar, Roll No. 214103437, has been carried out under my supervision for the fulfillment of Masters degree in the department of Mechanical Engineering, IIT Guwahati and this work has not been submitted elsewhere for any other degree.

Dr. Atanu Banerjee
Associate Professor
Department of Mechanical Engineering
Indian Institute of Technology Guwahati
June, 2023

Acknowledgment

<div align="right">
Yash Kumar
Roll No. 214103437
June 2023
IIT Guwahati
</div>

Abstract

Shape Memory Alloy (SMAs) are smart materials with the ability to undergo large deformation while loaded and recover their original shape after unloading or on heating above a specific temperature. These materials have been used in various applications such as in the field of aerospace, robotics, biomedical etc. To understand and model the thermomechanical response of SMAs, several constitutive models have been proposed and tested. Both in academia and industry, these models have been extensively used to design and analyze SMA based members and their behaviour.

During my study, in the first phase of work, finite element analysis of 2D elastic structures were carried out and validated. For this purpose, deal.ii software was used. In second phase of the project, Boyd and Lagodous constitutive model of SMA was understood and incorporated in FE code in order to study the response of pseudoelastic behaviour of SMA based members such as Beam and Spring. Obtained pseudoelastic respone was found to be in close agreement with that of the same in existing literature.

Contents

List of Figures

List of Tables

Nomenclature

M^d Detwinned Martensite

M^t Twinned Martensite

E^A Elastic Modulus of Austenite

E^M Elastic Modulus of Martenite

A_f Austenite Finish Temperature

A_s Austenite Start Temperature

M_s Martenite Start Temperature

M_f Martenite Finish Temperature

T_0 Reference Temperature

Y^* Critical value for thermodyanic force to cause transformation

ϕ Transformation Function

Θ Tangent Thermal Moduli Tensor

ϵ Uniaxial total Strain

$\epsilon^t r$ Uniaxial Transformation Strain

μ Poison's ratio

ξ Martensitic volume Fraction

π Thermodynamic Force Conjugate to ξ

σ_s^A Completion stress for Reverse Transformation into Austenite

σ_f^A Initiation stress for Reverse Transformation into Austenite

σ_f^M Completion stress for Reverse Transformation into Martenite

σ_s^M Initiation stress for Reverse Transformation into Martenite

$\boldsymbol{L}$ Tangent Stiffness Tensor

$\boldsymbol{S}$ Fourth-order Effective Compliance tensor

$\boldsymbol{S}^A$ Fourth-order Compliance tensor of Austenite

Λ Transformation Tensor

α Second-order Effective Thermal Expansion tensor

α^A Thermal expansion coefficient tensor of Austenite

α^M Thermal expansion coefficient tensor of Martenite

$f(\xi)$ Transformation Hardening Function

Abbreviations

FEA	Finite Element Analysis
SMA	Shape Memory Alloy
SME	Shape Memory Effect
PZT	Piezoelectric
BCC	Body-centred Cubic
FCC	Face-centered Cubic
DOF	Degree of Freedom
PE	Pseudoelasticity Effect
A	Austenite
M	Martenite
DM	Detwinned Martensite
E	Elastic Modulus
G	Gibb's Free Energy

Chapter 1

Introduction

1.1 Shape Memory Alloy

Shape memory alloy (SMA) is an extraordinary class of materials that possess the remarkable ability to "remember" and recover their original shape after being deformed. This unique characteristic is a result of their exceptional thermoelastic behavior, making them distinct from conventional metals. SMA materials can undergo significant deformations at certain temperatures, and upon exposure to a specific stimulus, such as heat or stress, they return to their predetermined shape.

The discovery of shape memory alloys dates back to the 1930s when a metallurgist named Arne Olander observed the unusual properties of an alloy composed of nickel and titanium. However, it wasn't until the 1960s that researchers began to extensively investigate these materials and unlock their full potential. Today, shape memory alloys are widely recognized and utilized in various fields, including aerospace, automotive, robotics, medicine, and consumer electronics.

One of the most captivating aspects of shape memory alloys is their ability to recover their original shape by either heating or applying stress to the material. Heating the SMA above its transformation temperature allows it to return to its austenitic phase, causing it to revert to its pre-deformed shape. Alternatively, applying mechanical stress to the SMA in its martensitic phase enables the material to recover its original shape upon heating, even if it is not deformed. The key driving force behind memory effect in these alloys is a reversible solid-state phase transformation. When the SMA is in its austenitic phase, it exhibits a high-temperature crystal structure with superior mechanical properties. Upon cooling below a specific temperature, known as the transformation temperature, the alloy undergoes a martensitic phase transformation, resulting in a reorientation of its crystal lattice and a deformation of the material.

The exceptional properties of shape memory alloys have made them immensely valuable in numerous practical applications. They are widely used in the aerospace industry for applications such as actuation systems, adaptive wing structures, and vibration damping.

In the medical field, SMA-based devices find applications in stents, orthodontic braces, and minimally invasive surgical tools. Additionally, they have been utilized in robotics, automotive engineering, and smart materials for their unique shape-changing abilities.

The exploration and development of shape memory alloys continue to expand, with ongoing research focused on refining their properties, enhancing their performance, and exploring new alloy compositions. The versatility and potential of these materials offer exciting possibilities for technological advancements and innovation in various industries, paving the way for a future where smart materials play a crucial role in enhancing our lives.
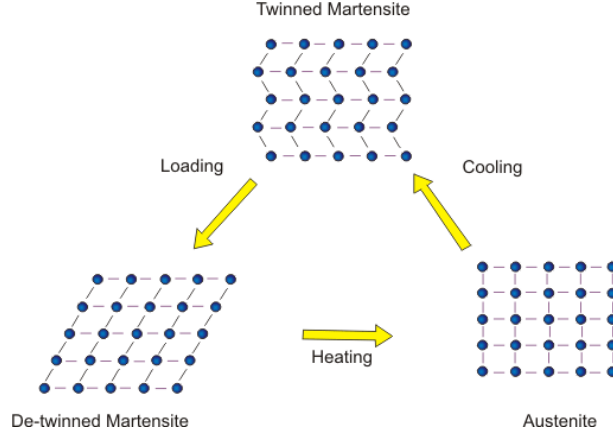
Figure 1.1: Phase transformation of SMA.

Shape memory alloys (SMAs) can undergo large strains and completely recover these strains under thermal and mechanical loading due to crystallographic phase transformations as shown in Figure 1.1. These transformations do not happen due to the diffusion of atoms but due to shear lattice distortions. These transformations are called martensitic phase transformations as they happen between austenite and martensite phase or vice versa. Depending upon the behaviour of loading, these phases can be categorized into Shape Memory Effect (SME) and Pseudoelasticity Effect (also referred as superelasticity).

1.1.1 Phases in Shape Memory alloy

SMAs habe two phases, Austenite (A) and Martensite (M), each with different crystal structures. These are described as below.

Martensite

Martensite is the low temperature phase of SMA. It can exist as two forms: *twinned* martensite (M^t) and *detwinned* martensite (M^d). Twinned martensite is formed by the combination of "self-accommodated" martensite crystal structure with different orientations called *variants* [2]. Detwinned Martensite is formed by the domination of a specific

variant. When SMA at high temperature is cooled under no stress condition, then the transformation starts at temperature M_s and is complete when the temperature reaches M_f as in Figure 1.2. The Martensite thus formed is twinned Martensite, and this transformation is called *forward transformation* and is reversible. If now the twinned Martensite formed is mechanically loaded, then detwinned, the transformation of M^t to M^d, will start when stress reaches σ_s^{cr} and the material will be completely transformed to detwinned Martensite when stress reaches σ_f^{cr} as in Figure 1.3. This transformation is characterized by large irreversible strains, and even upon unloading, the configuration does not recover its original shape.
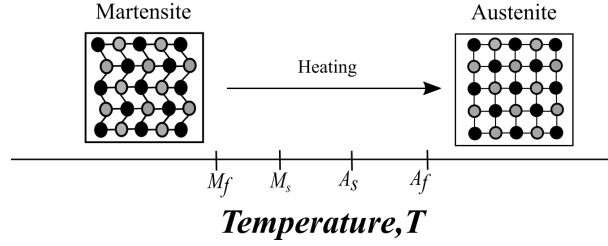
Figure 1.2: Temperature induced transformation of SMA without mechanical loading.
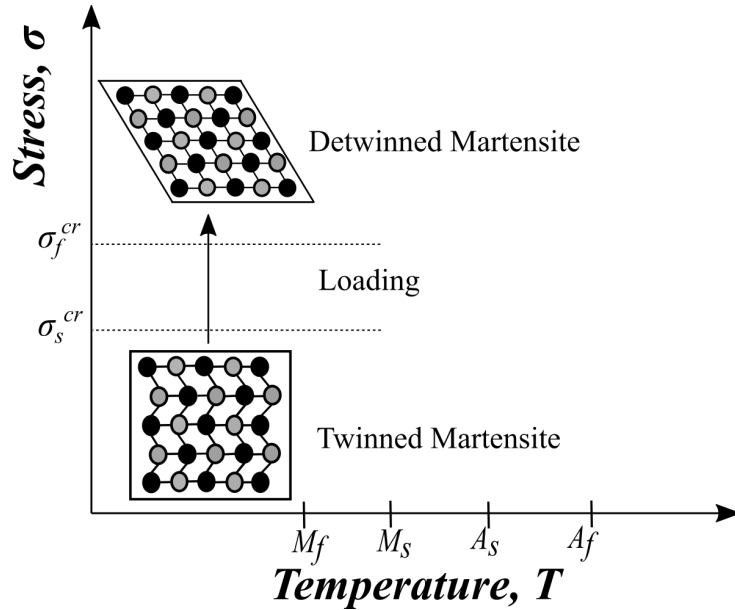
Figure 1.3: Transformation of twinned martensite to detwinned martensite under mechanical loading at temperature below M_f.

Austenite

Austenite is the high temperature phase of SMA having body-centered cubic (BCC) crystal structure. It offers higher elastic modulus than Martensite. When Martensite is heated transformation to Austenite starts at temperature A_s and is complete at temperature A_f
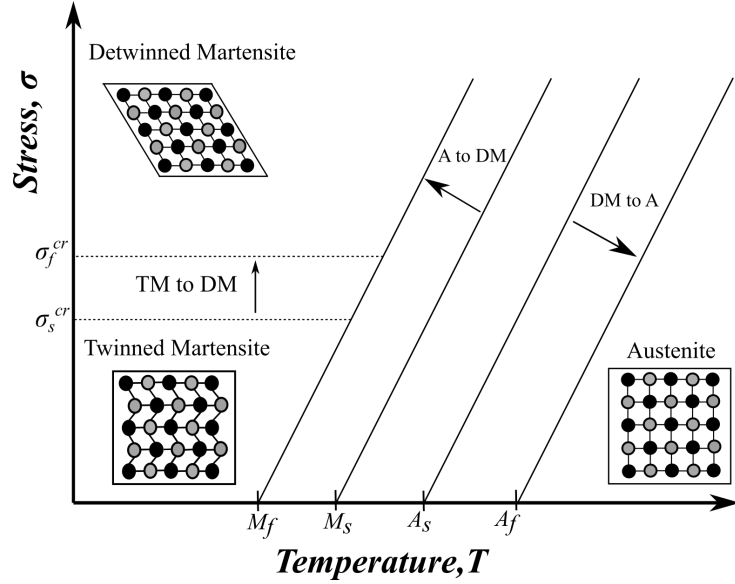
Figure 1.4: Schematic of stress-temperature phase diagram of an SMA.

as shown in Figure 1.4. This transformation is reversible and known as *reverse transformation*. Figure 1.5 shows the typical phase diagram for SMA depicting different phases and transformations.

1.2   Behaviour of SMA

Shape memory alloys (SMAs) exhibit fascinating behavior that sets them apart from conventional materials. Here is a short note on the behavior of shape memory alloys:

Shape Memory Effect: The most distinctive characteristic of SMAs is their ability to recover their original shape after being deformed. When the alloy is heated above its transformation temperature, it undergoes a reversible phase change from a lower temperature phase (martensitic) to a higher temperature phase (austenitic), allowing it to return to its pre-deformed shape.

Two-Way Shape Memory Effect: In addition to the one-way shape memory effect described above, some SMAs also exhibit a two-way shape memory effect. This means that they can recover their original shape not only by heating but also by applying mechanical stress while in the martensitic phase and then heating the material.

Superelasticity: SMAs possess remarkable elasticity, allowing them to undergo large deformations without permanent damage. This behavior is known as superelasticity or pseudoelasticity. Unlike traditional materials that would exhibit plastic deformation under stress, SMAs can recover their original shape completely upon the removal of the applied stress.

Temperature Sensitivity: The behavior of SMAs is highly sensitive to temperature changes. Their phase transformation and shape memory properties are influenced by the

4
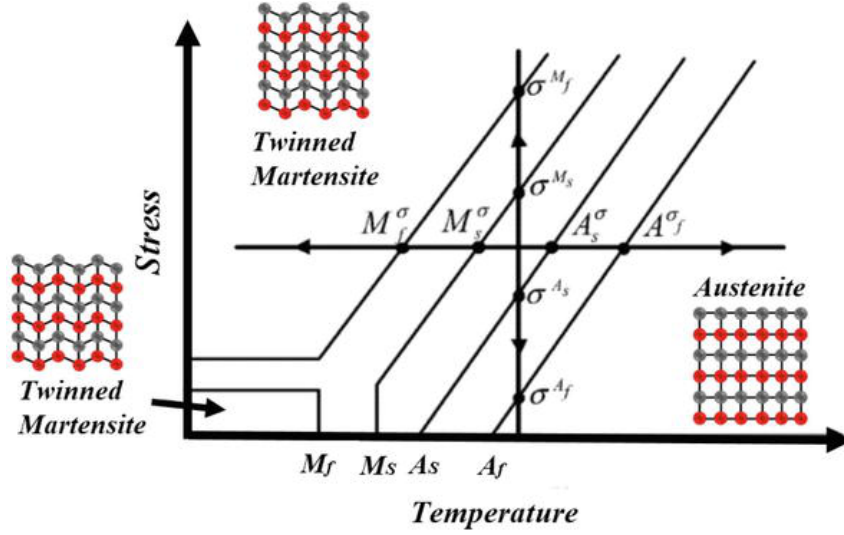
Figure 1.5: Schematic of stress-temperature phase diagram of an SMA.

temperature at which they are subjected to external stimuli. The transformation temperatures can be tailored during the alloy fabrication process to suit specific applications.

Hysteresis: When a shape memory alloy undergoes a phase transformation, there is often a temperature range over which the transformation occurs. This temperature hysteresis is due to the energy dissipation and structural changes within the material. The hysteresis effect can impact the performance and response time of shape memory alloy devices.

Fatigue and Aging: Like any material, SMAs are subject to fatigue and aging effects over time. Repeated cycling between the austenitic and martensitic phases can lead to fatigue and degradation of the material's shape memory properties. Careful design and control of the operating conditions are essential to ensure the long-term reliability and performance of shape memory alloy components.

Sensitivity to Alloy Composition: The behavior of SMAs is highly dependent on their alloy composition. Different combinations of elements, such as nickel, titanium, copper, and others, can be used to tailor the transformation temperatures, mechanical properties, and shape memory characteristics of the alloy to suit specific applications.

Understanding and harnessing the behavior of shape memory alloys have led to their widespread applications in various industries. From biomedical devices to aerospace components and consumer electronics, SMAs continue to pave the way for innovative technologies and solutions that benefit our daily lives. However, out of all these different behaviors of SMA, two properties are remarkably popular in research area, which are shape memory effect and pseudoelasticity.

1. Shape Memory Effect

The shape memory effect is a unique property exhibited by certain materials, particularly shape memory alloys (SMAs), which allows them to recover their original shape after deformation when subjected to certain external stimuli. The shape memory effect in SMAs is a result of a solid-state phase transformation that occurs within the material. These alloys typically exist in two distinct phases: the low-temperature phase (martensite) and the high-temperature phase (austenite). When the SMA is in its martensitic phase, it can be easily deformed into a different shape. However, upon exposure to an appropriate stimulus, such as heat or stress, the material undergoes a reversible phase transition, transforming from martensite to austenite. During this transition, the SMA recovers its original shape, effectively exhibiting the shape memory effect.

The specific triggering mechanism for the shape memory effect depends on the type of SMA and its composition. In the case of temperature-induced shape memory alloys, heating the material above a certain transition temperature, known as the austenite finish temperature, causes the phase transformation from martensite to austenite, enabling the material to regain its initial shape. Conversely, cooling the alloy below the austenite start temperature causes it to transform back into the martensitic phase, allowing for shape deformation once again.
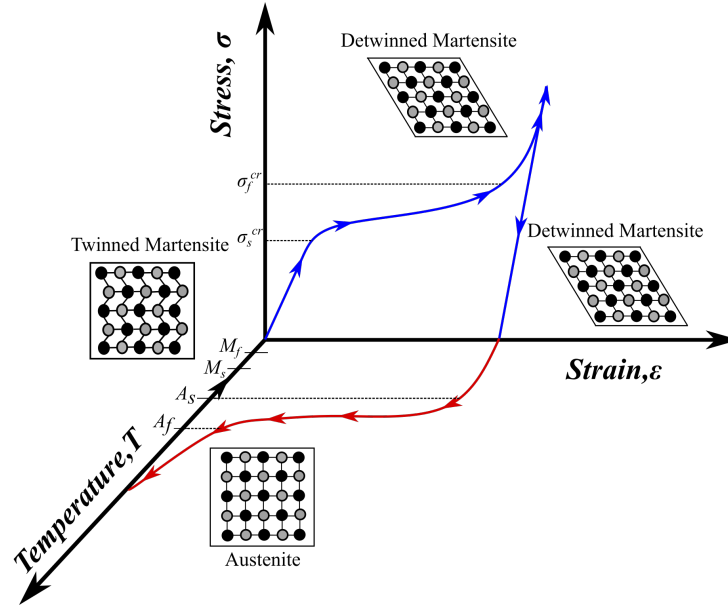
Figure 1.6: Stress-Strain-Temperature curve describing the shape memory effect for a typical NiTi SMA.

When SMA in twinned martensite phase is loaded above σ_f^{cr} it transforms to detwinned Martensite due to detwinning. This transformation is accompanied by large strains. When unloaded, SMA behaves elastically offering large residual strain. When heated above Austenite start temperature (A_s) transformation from Martensite to Austenite starts

and completes at Asutenite Finish temperature (A_f). Strain is completely recovered at this point. This phenomenon of undergoing large deformations upon loading and subsequent recovery when heated is termed as Shape Memory Effect and can be visualized by Figure 1.6. Decreasing the temperature below Martensite finish temperature (M_f) will cause forward transformation but there will be no macroscopic changes.

2. Pseudoelasticity

Pseudoelasticity is a remarkable effect observed in shape memory alloys, which are metallic materials capable of recovering their original shape after deformation when subjected to certain external stimuli, such as temperature changes or mechanical stress. The pseudoelasticity effect is a key characteristic of SMAs and distinguishes them from conventional metals.
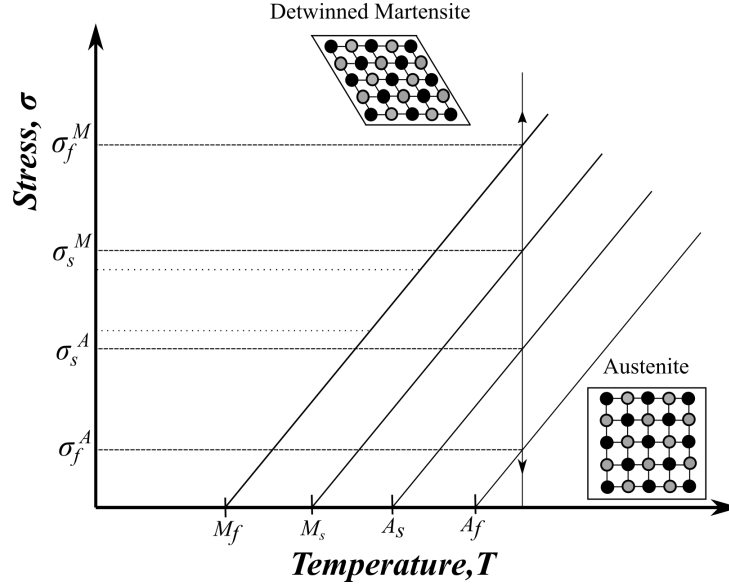
Figure 1.7: Phase diagram and the loading path during pseudoelastic behaviour of SMA.

When an SMA is deformed at a temperature below its transformation temperature, it exhibits an elastic response similar to other metals. However, unlike conventional metals, when an SMA is deformed at a temperature above its transformation temperature, it undergoes a reversible phase transformation known as austenite-to-martensite, resulting in a unique mechanical behavior. As shown in Figure 1.7 At high temperature (above A_f) where the austenite phase is stable upon loading the behaviour is elastic till σ_s^M. Above σ_s^M, Austenite directly transforms to detwinned Martensite. And above σ_f^M it is completely M^d. Further loading results in elastic strains of M^d. Upon unloading, elastic behaviour is observed till σ_s^A where M^d transformations to A and complete transformation strain is recovered when stress reaches σ_s^A. Further unloading recovers elastic strain in austenite phase. During the deformation in the martensitic phase, SMAs can undergo

7

large strains without permanent deformation. This behavior is known as the pseudoelasticity effect. When the external force is removed, the SMA spontaneously reverts to its original shape as it undergoes the reverse martensitic-to-austenite phase transformation. During this transformation, it dissipates some amount of energy which is called hysterisis. Figure 1.8 shows the hysteresis behaviour of SMA.
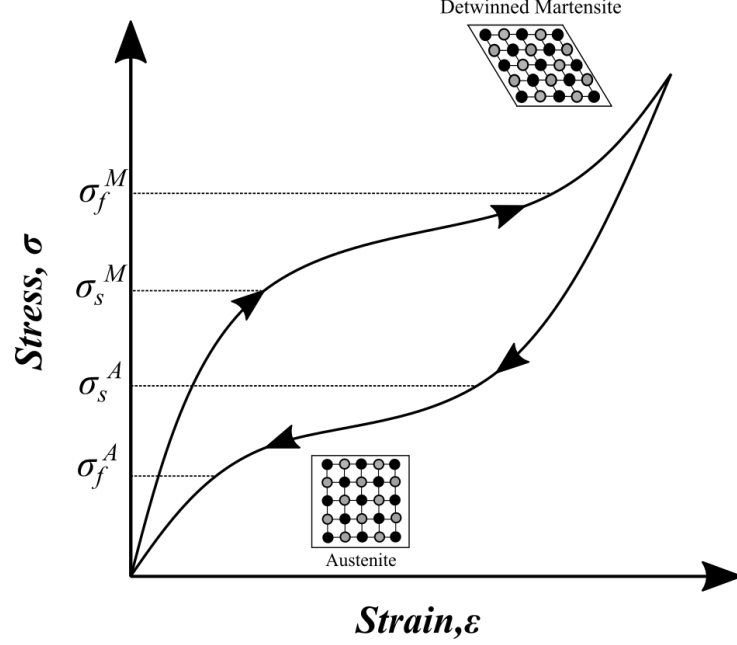
Figure 1.8: Stress-strain curve showing the hysteresis behaviour of SMA.

The pseudoelasticity effect is due to the rearrangement of the internal crystal structure within the SMA. The phase transformation between austenite and martensite involves a change in crystal lattice structure and reorientation of the internal crystallographic planes. This structural rearrangement allows SMAs to absorb and release significant amounts of strain energy, leading to their remarkable shape memory and pseudoelastic behavior.

The pseudoelasticity effect of SMAs has numerous practical applications. It is utilized in industries such as aerospace, automotive, robotics, and biomedical engineering. SMAs are used in various applications, including actuators, sensors, medical stents, orthodontic wires, and deployable structures. The ability of SMAs to undergo reversible, large deformations without permanent damage makes them ideal for applications requiring precise control, resilience, and shape memory capabilities. Among various SMA members that are used in several application, SMA spring is one of the most suitable in various application.

1.3 Shape Memory alloy spring

A shape memory alloy (SMA) spring is a remarkable engineering component that leverages the unique properties of SMAs to provide superior functionality in various applications. Shape memory alloy springs are designed using a SMA material, typically nickel-titanium

(NiTi) or copper-based alloys. These materials possess the extraordinary ability to recover their original shape, making them ideal for spring applications where deformation and subsequent recovery are required. The behavior of shape memory alloy springs is based on the shape memory effect and superelasticity exhibited by SMAs. When the spring is subjected to a force or temperature change, it undergoes a reversible phase transformation between the austenitic and martensitic phases of the alloy. This transformation allows the spring to deform and then recover its original shape once the external stimulus is removed.

Shape memory alloy springs offer several advantages over traditional metal springs. Firstly, they can undergo significantly larger deformations without permanent damage, thanks to the superelastic behavior of SMAs. This makes them highly resilient and durable, capable of withstanding repeated cycles of deformation and recovery and secondly, shape memory alloy springs provide excellent fatigue resistance. They can endure millions of cycles without significant loss of performance or deformation, making them suitable for applications that require high cycle life and reliability. Moreover, shape memory alloy springs offer precise control over their shape recovery. By carefully selecting the alloy composition and processing parameters, the transformation temperatures of the SMA can be tailored to match specific requirements. This allows engineers to design springs that exhibit the desired recovery behavior at specific temperatures or under specific applied forces.

Shape memory alloy springs find applications in a wide range of industries. They are commonly used in medical devices, such as surgical instruments, orthodontic braces, and stents, where the ability to recover their original shape is crucial. Additionally, they are utilized in aerospace and automotive systems, robotics, consumer electronics, and many other fields that require compact, reliable, and efficient mechanical components.

1.4   Literature Review

In this section, the history and applications of shape memory alloy are discussed. A review of various thermomechanical constitutive models available in the literature is presented. Various research works on the utilization of sma based actuators have been discussed extensively.

1.4.1   History of SMA

Shape memory alloys are such special materials which can "remember" their shape when heated above a certain transition temperature Jani et al. [3]. The discovery of martensite in steel led to discovery of shape memory alloys. Martensite transformations which initially considered irreversible, can be reversed and thus scientists were able to obtain two different structures. Shape Memory alloy was first discovered by Arne Olande. He

observed the shape and recovery ability of a gold-cadmium alloy (Au-Cd). Later scientists from US naval Ordinance Laboratory observed the shape memory effect in a nickel and titanium alloy, which is known as "nitinol". [4] observed that NiTi exhibited good mechanical properties and also possessed shape recovery capability, which was termed as shape memory effect. In 1965, Wang et al. [5] showed that a drastic decrease in SMA transformation temperatures occurs by the addition of elements such as Co and Fe to the existing NiTi system. this new alloy found application as pipe coupling, known as Cryoft, in F-14 aircraft.

1.4.2 Applications of SMA

Shape memory properties of SMA have led to extensive research and eventual use in various engineering fields.

Aerospace Applications

Costanza and Tata [6] in his paper discussed about diverse applications of shape memory alloys (SMAs) in the aerospace field, with a particular focus on morphing wings . Both experimental investigations and modeling studies have been conducted to explore the use of SMAs in this area. Morphing wings offer the potential for improved aerodynamic performance and fuel efficiency by adapting their shape to varying flight conditions.

Additionally, SMAs are utilized in tailoring the orientation and geometry of inlet systems in propulsion systems. By optimizing these parameters, the efficiency of propulsion systems can be enhanced, resulting in improved performance and reduced power consumption. Variable geometry chevrons are another application of SMAs in aerospace. These chevrons are used for both thrust optimization and noise reduction. By dynamically adjusting the geometry of the chevrons using SMAs, the performance of jet engines can be optimized for different operating conditions.

Kudva [7] through his paper depicted that, to optimize the performance of lifting bodies, SMA wire-tendons could be used to actuate hingeness ailerons by a collaboration between DARPA, AFRL, and Northrop named smart wing program . Variable geometry airfoil that changed the airfoil configuration from symmetric to cambered through SMA actuation was developed by Strelec et al. Martensitic transformation can provide changing elastic stiffness which led to research in the area of dynamic property optimization of aircraft structural panels. It was found that pre-straining the SMA or increasing the volume fraction of SMA fibers can decrease the thermally induced post-buckling deflection of a structure [8].

SMAs also find application in space-related activities. They can be employed to isolate micro-vibrations, which is crucial for sensitive instruments and equipment in space missions. Furthermore, SMAs are utilized in low-shock release devices and self-deployable

solar sails, enabling efficient and controlled deployment of various components and structures in space. The aerospace field continually explores novel configurations and devices utilizing SMAs. These advancements aim to improve performance, efficiency, and reliability in various aerospace applications, including aircraft and spacecraft. [9] and [10] conducted several studies for better control of rotor blade by reducing vlade-vortex interaction.

Biomedical Applications

A material to used in the human body must be bio-compatible i.e. remains nontoxic through its functional period. The biocompatibility of NiTi along with Shape memory effect and Pseudoelasticity makes it a suitable candidate for biomedical applications. For orthopedic applications, porous SMAs are used as artificial bone implants [11]. Porous nature of these materials enables the bone tissue to migrate inward and increase bond strength. In cardiovascular field, SMAs aro used as Simon filter that traps the clots in the blood stream .30]. The filter is deployed in the blood stream in contracted form and it expands after implantation as of tho temperature is higher than T_s^A. NiTiNoL based archwires have been used in orthodontic applications since 1970s [12].

SMA can be used as Bone plates - Surgical tools to assist healing of broken bones. Bone plates of SMA are cooled, inserted, and body temp causes contraction and plate maintains pressure for proper healing.

Petrini and Migliavacca [13] in his paper "Biomedical Applications of Shape Memory Alloys" mentions various applications of SMA in Orthopedic field, Vascular Field and Neurosurgical Field. The discovery of shame memory alloy's property boosted the development of mini-invasive techniques where the pathology is treated by the percutaneous insertion of the device rather than surgical intervention. Similarly, NiTi alloys in the neurosurgical field are used for producing three typed of devices such as coils, stents and microguidewires.

Kauffman and Mayo [14] publishes his paper "The Story of Nitinol: The Serendipitous Discovery of the Memory Metal and Its Applications" in which he studies the revolutionizing properties of NiTiNol alloy and its various applications in biomedical field such as orthopedic and cardiovascular surger, orthodontics.

Transportation Applications

The transportation industry is facing the challenge of achieving sustainable growth in the new century. To address this challenge, the development of new materials and technologies is crucial, leveraging the unexpected properties that these materials can offer. The emergence of mechatronics has opened the door to a paradigm shift in the transportation industry, introducing the use of smart materials.

San Juan [15] in his paper "Application of shape memory alloys to the transport industry" showcased that smart materials have the potential to provide new functional properties and design capabilities that were previously unforeseen. Among the various types of smart materials, Shape Memory Alloys (SMA) hold significant promise. This is primarily due to their unique thermo-mechanical properties, such as superelasticity and shape memory effects. Additionally, SMAs possess the ability to perform work and damp vibrations.

The specific properties of SMAs make them excellent candidates for a wide range of applications. They can be used as sensors and actuators, enabling the development of advanced control systems. SMAs are also effective in active and passive damping applications, where they can attenuate vibrations and enhance vehicle stability. Furthermore, SMAs can serve as removable fasteners for assembly and disassembly processes, offering convenience and flexibility.

Shreekrishna et al. [16] in his paper "A review on shape memory alloys and their prominence in automotive technology" discussed how SMA actuators have emerged as a prevalent automotive application for shape memory alloys (SMA) . These compact and lightweight actuators serve as efficient alternatives to traditional mechanical actuators, offering several advantages such as silent operation, enhanced reliability, durability, and resistance to environmental factors like humidity, shock, and vibrations. In the automotive industry, SMA actuators find application in a wide range of systems. They are utilized in adjustable mirrors, windshield wipers, door locks, smart bonnets, tumble flaps, governor valves, fog louvers, hatch vents, and various other components. These actuators enable precise and reliable control of these systems, contributing to improved functionality and user experience.

1.4.3 Constitutive Models of SMA

A constitutive model is a mathematical representation that describes the behavior of a material under various loading conditions. In the context of shape memory alloys (SMAs), which are a class of materials with unique shape-changing properties, a constitutive model is used to predict their mechanical response.

A constitutive model for shape memory alloys considers the material's inherent properties, such as phase transformation and mechanical behavior, and incorporates them into a set of equations or algorithms. These models aim to capture the complex relationship between stress, strain, temperature, and other variables that govern the SMA's response. The most common constitutive model for shape memory alloys is based on thermodynamics and typically involves the use of a set of material parameters. These parameters describe the SMA's thermal and mechanical properties, including transformation temperatures, elastic moduli, and transformation strains.

Paiva and Savi [17] in his paper "An overview of constitutive model for shape

memory alloys" discusses that constitutive models for shape memory alloys may include various elements such as linear or nonlinear elasticity, plasticity, and viscoelasticity, depending on the specific behavior being modeled. Additionally, these models often consider the effects of thermal cycling, stress-induced transformations, and strain-rate dependence . Developing accurate constitutive models for shape memory alloys is crucial for understanding and predicting their behavior in practical applications. These models are used in engineering simulations and design processes to optimize the performance of shape memory alloy components and systems in fields such as aerospace, robotics, biomedicine, and smart structures.

Tanaka [18] proposed the phenomenological model for SMA, assuming material parameters such as elastic modulus, coefficient of thermal expansion and transformation tensor, to be constant and taking martensite volume fraction (ξ) as an internal variable. Here, ξ, varies with temperature and stress. In this model, exponential rule is proposed, to relate the martensite volume fraction with stress and temperature. Liang and Rogers [19] adopted the same constitutive law, as that of Tanaka's Model. However, the phase kinetics are expressed in terms of cosine functions instead of exponential function to avoid numerical complexity. In both the above-defined model martensite volume fraction (ξ) varies from "1", complete martensite to "0" complete austenite phase and vice versa. One of the most important limitation of these two models was, they were capable of explaining only the pseudoelasticity effect, but not the shape memory effect. In the year 1993, Brinson [20] modified this constitutive relation by redefining the martensite volume fractions as a new internal state variable. The martensite phase is divided into two components, as temperature induced or twinned martensite (ξ_T), and stress induced or detwinned martensite (ξ_S). Thus, the total martensite fraction ξ can be written as $\xi = \xi_S + \xi_T$. Bekker and Brinson [21] further proposed that martensite volume fraction (ξ) did not only depend on the current stress and temperature state, but also on the past thermomechanical loading path. In order to simulate that they reported that phase transformation at a point of loading path occurs only if the direction of loading path has a component in the direction of transformation and the amount of phase transformation is proportional to the distance travelled along the loading direction. They introduced a switching point that distinguishes the portion of the path, where the transformation is active, from the rest of the loading path where transformation is inactive.

Boyd and Lagoudas [2] modelled pseudoelsticity and shape memory effect (SME) as an effect of martensitic transformation and reorientation using free energy function and a dissipation potential. Three cases were considered along with austenite for analysis, viz. one type of martensite, two type of martensite, variable number of martensite variants. Closed form equations were derived using laws of thermodynamics. Residual stresses due to heterogeneity was accounted by this model by specifying back and drag stress. This model was able to simulate partial and inner hysteresis loops including cyclic loading.

Lagoudas et al. [22] proposed a unified thermodynamic constitutive model based on

Gibbs free energy structure associated with martensitic volume fraction. Various hardening functions are proposed in terms of martensitic volume fraction and various material functions to account for different transformation induced strain hardening. Also, they implemented this constitutive model in a incremental displacement based finite element scheme using return mapping algorithm to simulate active metal matrix composite embedded with SMA fibers.

Bo and Lagoudas [23] proposed a constitutive model for cyclic loading of SMA, because plastic strain gets accumulated for every transformation cycle. They considered plastic strain (ϵ_p), back stress (β), and drag stress (η) with martensitic volume fraction (ξ). The evolution of transformation strain, back and frag stress is represented as a function of ξ. This work was further extended by Qidwai and Lagoudas [24] for numerical implementation of SMA thermomechanical stress-strain response using elastic predictor-transformation corrector algorithm. An implicit scheme (closest point projection algorithm) and explicit scheme (convex cutting plane algorithm) were implemented for transformation correction. In 2012, Lagoudas et al. [22] proposed 3 improvements of this constitutive model of phase transformation in SMAs viz. (i) capability to account for the smooth transition of thermal and mechanical responses at the time of initiation and completion of martensitic transformation, (ii) able to capture the generation of favored martensitic variants, resulting in applied stress magnitude without specifically accounting for martensitic reorientation, thus making it a computationally efficient and accurate analysis tool, (iii) generalisation of the concept of the critical thermodynamic forces for transformation, which become dependent on the applied stress magnitude and the direction of transformation.

Liang and Rogers [25] In this research paper, a comprehensive thermomechanical constitutive model is proposed for shape memory alloys (SMAs) that incorporates both micromechanical and macromechanical aspects. The model introduces the martensite fraction as a variable to capture the martensitic transformation, which is responsible for the unique properties of SMAs. This constitutive model enables the study of complex behaviors exhibited by two-dimensional (2-D) and three-dimensional (3-D) SMA structures. Additionally, the paper presents a simple example using this constitutive model, uncovering a novel and intriguing phenomenon observed in 3-D SMA structures.

He et al. [26] published the paper called "Comprehensive shape memory alloys constitutive models for engineering application". In the paper, practical constitutive models for shape memory alloys (SMA) are proposed to enable accurate engineering calculations. These models are applicable to both single loading-unloading processes and multiple loading-unloading cycles. The authors introduce a more accurate SMA theoretical tensile curve and temperature-stress phase transformation diagram to derive the constitutive model. By incorporating these improved representations, the proposed model can provide more precise predictions of the material's behavior. One notable aspect of the proposed constitutive model is its consideration of the incomplete phase transformation

phenomenon, which occurs when the material does not fully undergo phase transformation during loading and unloading cycles. The model also accounts for the variation of the critical phase transformation stress under multiple loading and unloading conditions. This consideration enables a more accurate evaluation of the critical phase transformation stress and stress-strain relationships at various temperatures. To validate the proposed model, the researchers conducted tensile tests under various working conditions. These experiments likely involved subjecting SMA specimens to different temperature and loading conditions to assess their mechanical response. The obtained experimental data were then compared with the predictions of the proposed constitutive model to evaluate its accuracy and applicability in practical engineering calculations.

Cisse et al. [27] published his paper titled "A review of constitutive models and modeling techniques for shape memory alloys". The objective of this paper is to present a comprehensive and current review of the main constitutive models used for shape memory alloys (SMA), tracing their development from their initial formulations to their latest iterations. The paper organizes these models based on the approaches they employ to describe the behavior of SMAs.

1.5   Scope of Study

The scope of study in shape memory alloys (SMAs) is broad and encompasses various aspects related to their material properties, behavior, applications, and manufacturing processes. Here are some key areas within the scope of study in SMAs:

Material Characterization: This involves investigating the composition, microstructure, mechanical properties, and phase transformation behavior of SMAs. It includes techniques such as microscopy, spectroscopy, and mechanical testing to understand the material's structure and properties.

Constitutive Modeling: Developing accurate mathematical models and constitutive equations to describe the complex behavior of SMAs under different loading and temperature conditions. This involves understanding phase transformations, stress-strain relationships, hysteresis effects, and incorporating them into computational models.

Thermomechanical Behavior: Analyzing the response of SMAs to thermal and mechanical stimuli, including their shape memory effect, superelasticity, and pseudoelasticity. This includes studying the effects of temperature, stress, strain rates, and environmental factors on the material's behavior.

Applications and Devices: Exploring the wide range of applications for SMAs, such as aerospace, automotive, biomedical, and robotics. This involves designing and developing SMA-based devices, actuators, sensors, and structures for specific functionalities, including morphing structures, energy absorption, vibration damping, and adaptive systems.

1.6 Objective of Study

Objectives of the study are as follows:

1. Development of finite element tool to study the response of elastic members.

2. Implementation of the SMA constitutive model into nonlinear finite element formulation to simulate the behavior of SMA based members under mechanical loading.

1.7 Organization of the Report

The report has been organized as follows: **Chapter 1** offers some background on the Shape memory alloy, and its applications. Different shape memory alloy constitutuve models available in the literature are also discussed. Based on this, the scope and objective of the present study were defined. In **Chapter 2**, theory related to finite element analysis were discussed and a few elastic 2D and 3D problems were solved under tensile loading-unloading. In **Chapter 3**, the thermomechanical constitutive model of Shape memory alloy proposed by Boyd and lagodous [2] is presented, which is used for the current study and analysis of SMA beam, spring and torque-tube were carried out. The results obtained are compared with the results available in the literature for validation. **Chapter 4** concludes the present work and discusses the future scope.

Chapter 2

Finite Element Analysis

Finite element method (FEM) is a numerical method for solving a differential or integral equation. It is applied to a number of physical problems, where the governing differential equations are available. The method essentially consists of assuming the piecewise continuous function for the solution and obtaining the parameters of the functions in a manner that reduces the error in the solution. In this section, a brief introduction to finite element method is provided. The method is illustrated with the help of the plane stress and plane strain formulation.

2.1 Finite Element formulation

2.1.1 2.1 Voight Notation

In case of 2D, the strain vector is represented as

$$\boldsymbol{\epsilon}(\boldsymbol{u}) = \left\{ \begin{array}{c} \epsilon_x \\ \epsilon_y \\ \gamma_{xy} \end{array} \right\} = \left\{ \begin{array}{c} \frac{\partial u_x}{\partial x} \\ \frac{\partial u_y}{\partial y} \\ \frac{\partial u_x}{\partial y} + \frac{\partial u_y}{\partial x} \end{array} \right\}, \tag{2.1}$$

where the displacement vector is defined as

$$\boldsymbol{u} = \left\{ \begin{array}{c} u_x(x,y) \\ u_y(x,y) \end{array} \right\}. \tag{2.2}$$

Here, u_x and u_y are the displacements in X- and Y- directions. Equation 2.1 can be rewritten as

$$\boldsymbol{\epsilon} = \begin{bmatrix} \frac{\partial}{\partial x} & 0 \\ 0 & \frac{\partial}{\partial y} \\ \frac{\partial}{\partial y} & \frac{\partial}{\partial x} \end{bmatrix} \left\{ \begin{array}{c} u_x \\ u_y \end{array} \right\}. \tag{2.3}$$

In matrix notation

$$\boldsymbol{\epsilon} = \boldsymbol{\nabla}_s \boldsymbol{u}. \tag{2.4}$$

17

$$\left.\frac{\partial u}{\partial n}\right|_{\Gamma_2} = g$$

$$\Omega$$

$$u\big|_{\Gamma_1} = u_0$$
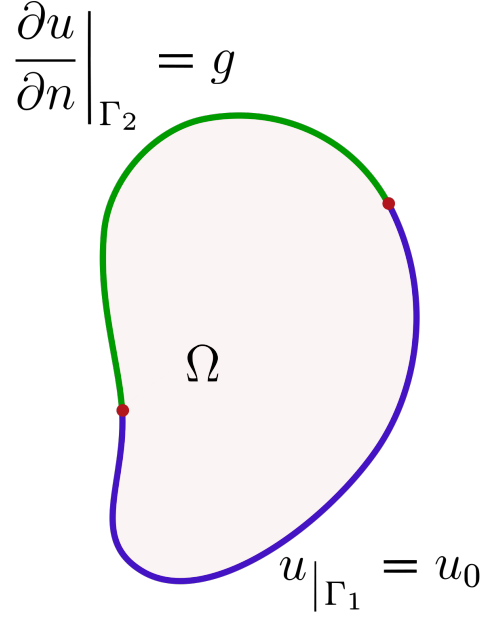
Figure 2.1: Schematic representation of the domain.

Here $\boldsymbol{\nabla}_s$ is symmetric gradient of displacement. The corresponding stress tensor $\boldsymbol{\sigma}$ can be expressed as the stress vector as,

$$\boldsymbol{\sigma} = \begin{Bmatrix} \sigma_{xx} \\ \sigma_{yy} \\ \sigma_{xy} \end{Bmatrix}. \tag{2.5}$$

For plane stress conditions and linear elastic material, the stress and strain vectors are related by the constitutive equation,

$$\boldsymbol{\sigma} = \boldsymbol{D}\boldsymbol{\epsilon},$$

$$\text{where, } \boldsymbol{D} = \frac{E}{1-\nu^2} \begin{bmatrix} 1 & \nu & 0 \\ \nu & 1 & 0 \\ 0 & 0 & \frac{1-\nu}{2} \end{bmatrix}. \tag{2.6}$$

E represents the Modulus of elasticity, and ν is the poison's ratio.

2.1.2 Equilibrium Equation

Considering an open domain Ω with boundary Γ, composed of two distinct boundaries, a Dirichlet boundary Γ_1 and Neumann boundary Γ_2, as shown in Figure 2.1. The equilib-

18

rium equations along X- and Y- directions are obtained as,

$$\frac{\partial \sigma_{xx}}{\partial x} + \frac{\partial \sigma_{yx}}{\partial y} + f_x = 0,$$
$$\frac{\partial \sigma_{xy}}{\partial x} + \frac{\partial \sigma_{yy}}{\partial y} + f_y = 0. \tag{2.7}$$

Where, σ_{ij} represents stress on i^{th} plane in j direction, f_x and f_y represents the body force vector along X- and Y- directions. As the model is assumed to be isotropic, $\sigma_{xy} = \sigma_{yx}$. Combining the Equation 2.7 into matrix form yield,

$$\begin{bmatrix} \frac{\partial}{\partial x} & 0 & \frac{\partial}{\partial y} \\ 0 & \frac{\partial}{\partial y} & \frac{\partial}{\partial x} \end{bmatrix} \begin{Bmatrix} \sigma_{xx} \\ \sigma_{yy} \\ \sigma_{xy} \end{Bmatrix} + \begin{Bmatrix} f_x \\ f_y \end{Bmatrix} = \begin{Bmatrix} 0 \\ 0 \end{Bmatrix}. \tag{2.8}$$

The equilibrium equation be represented as,

$$\boldsymbol{\nabla}_s^T \boldsymbol{\sigma} + \boldsymbol{f} = \boldsymbol{0} \quad \text{in} \quad \Omega.$$

subjected to the boundary conditions, $\tag{2.9}$

$$\boldsymbol{u} = \boldsymbol{g} \quad on \quad \Gamma_D, \; \boldsymbol{\sigma} \cdot \boldsymbol{n} = \boldsymbol{h} \quad on \quad \Gamma_N.$$

The equilibrium equations with the boundary conditions constitutes the **strong form** of the model. Here, $\boldsymbol{f} = \begin{Bmatrix} f_x \\ f_y \end{Bmatrix}$ represents the body force vector on the model, $\boldsymbol{n}$ represents outward normal and $\boldsymbol{h}$ is the external traction on the Neumann boundary Γ_N.

2.1.3 Weak Form

The strong form is converted to weak form by substituting the test function, $\boldsymbol{u}(x,y) = \begin{Bmatrix} u_x(x,y) \\ u_y(x,y) \end{Bmatrix}$ into the strong form Equation 2.7, and the residue is obtained as

$$R_x = \sigma_{xx,x} + \sigma_{yx,y} + f_x,$$
$$R_y = \sigma_{xy,x} + \sigma_{yy,y} + f_y. \tag{2.10}$$

Where R_x and R_y are residue in X- and Y- directions respectively, and $\boldsymbol{\sigma}_{ij,j} = \frac{\partial \boldsymbol{\sigma}_{ij}}{\partial x_j}$. Minimizing the residues by multiplying with corresponding weight functions and integrating over the domain yields,

$$\int_\Omega (R_x w_x + R_y w_y) \, d\Omega = 0. \tag{2.11}$$

By expanding the above equation,

$$\int_\Omega \{(\sigma_{xx,x} + \sigma_{xy,y} + f_x)w_x + (\sigma_{xy,x} + \sigma_{yy,y} + f_y)w_y\} \, d\Omega = 0. \tag{2.12}$$

19

Rewriting the Equation 2.12,

$$\int_\Omega \{\frac{\partial}{\partial x}(\sigma_{xx}w_x) + \frac{\partial}{\partial y}(\sigma_{xy}w_x) + \frac{\partial}{\partial x}(\sigma_{xy}w_y) + \frac{\partial}{\partial y}(\sigma_{yy}w_y)\}\, d\Omega -$$
$$\int_\Omega \{\sigma_{xx}w_{x,x} + \sigma_{xy}w_{x,y} + \sigma_{xy}w_{y,x} + \sigma_{yy}w_{y,y}\}\, d\Omega + \int_\Omega \{f_x w_x + f_y w_y\}\, d\Omega = 0. \tag{2.13}$$

By incorporating the del operator $\boldsymbol{\nabla}$, Equation 2.13 is expressed as

$$\int_\Omega \left[\boldsymbol{\nabla} \begin{Bmatrix} \sigma_{xx}w_x \\ \sigma_{xy}w_x \end{Bmatrix} + \boldsymbol{\nabla} \begin{Bmatrix} \sigma_{xy}w_y \\ \sigma_{yy}w_y \end{Bmatrix}\right] d\Omega + \int_\Omega \{f_x w_x + f_y w_y\}\, d\Omega =$$
$$\int_\Omega \{\sigma_{xx}w_{x,x} + \sigma_{xy}w_{x,y} + \sigma_{xy}w_{y,x} + \sigma_{yy}w_{y,y}\}\, d\Omega. \tag{2.14}$$

Applying the Gauss-divergence theorem,

$$\int_\Omega \{\sigma_{xx}w_{x,x} + \sigma_{xy}w_{x,y} + \sigma_{xy}w_{y,x} + \sigma_{yy}w_{y,y}\}\, d\Omega = \int_\Omega \{f_x w_x + f_y w_y\}\, d\Omega +$$
$$\int_{\Gamma_N} \{(\sigma_{xx}w_x + \sigma_{xx}w_y)n_x + (\sigma_{xy}w_x + \sigma_{yy}w_y)n_y\}\, d\Gamma_N. \tag{2.15}$$

By using the definition of strain from Equation 2.1, one can get the weak form as

$$\int_\Omega \{\boldsymbol{\epsilon}(\boldsymbol{w})\}^T \{\boldsymbol{\sigma}\}\, d\Omega = \int_\Omega \boldsymbol{w}^T \boldsymbol{f}\, d\Omega + \int_{\Gamma_N} \boldsymbol{w}^T \boldsymbol{h}\, d\Gamma_N. \tag{2.16}$$

Where, $\boldsymbol{w} = \begin{Bmatrix} w_x \\ w_y \end{Bmatrix}$. By incorporating the symmetric gradient operator (Equation 2.31) and the constitutive equation (Equation 2.6), one gets

$$\int_\Omega (\boldsymbol{\nabla}_s \boldsymbol{w})^T \boldsymbol{D}(\boldsymbol{\nabla}_s \boldsymbol{u})\, d\Omega = \int_\Omega \boldsymbol{w}^T \boldsymbol{f}\, d\Omega + \int_{\Gamma_N} \boldsymbol{w}^T \boldsymbol{h}\, d\Gamma_N. \tag{2.17}$$

The above Equation 2.17 is the weak form of the strong form Equation 2.9.

2.1.4   Discretization of Weak Form

The displacement field of the domain can be expressed as

$$u_x = \sum_{i=1}^n u_{xi} R_i(\xi, \eta),$$
$$u_y = \sum_{i=1}^n u_{yi} R_i(\xi, \eta).$$

where R_i represents the ith element. Expressing the above equations in matrix notation,

$$\boldsymbol{u} = \begin{bmatrix} R_1 & 0 & R_2 & 0 & \cdots & R_n & 0 \\ 0 & R_1 & 0 & R_2 & \cdots & 0 & R_n \end{bmatrix} \begin{Bmatrix} u_{x1} \\ u_{y1} \\ u_{x2} \\ u_{y2} \\ \vdots \\ u_{xn} \\ u_{yn} \end{Bmatrix}.$$

or

$$\boldsymbol{u} = [\boldsymbol{N}_e]\{\boldsymbol{d}_e\}. \tag{2.18}$$

Here $\boldsymbol{N}_e$ and $\boldsymbol{d}_e$ represent the shape function matrix and degrees of freedom of an element. The degrees of freedom of an element $\boldsymbol{d}_e$ and the global degrees of freedom $\boldsymbol{d}$ are related as,

$$\{\boldsymbol{d}_e\} = [\boldsymbol{L}_e]\{\boldsymbol{d}\} \tag{2.19}$$

Following the Galerkin approach, the weight function can be expressed as,

$$\boldsymbol{w} = [\boldsymbol{N}_e]\{\boldsymbol{\beta}_e\} \tag{2.20}$$

From Equation 2.19 and (2.20), the symmetric gradient operator of $\boldsymbol{u}$ and $\boldsymbol{w}$ are obtained as,

$$\begin{aligned} \nabla_s \boldsymbol{u} &= [\boldsymbol{B}_e][\boldsymbol{L}_e]\{\boldsymbol{d}\}, \\ \nabla_s \boldsymbol{w} &= [\boldsymbol{B}_e][\boldsymbol{L}_e]\{\boldsymbol{\beta}\}, \end{aligned} \tag{2.21}$$

where,

$$\boldsymbol{B}_e = \begin{bmatrix} R_{1,x} & 0 & R_{2,x} & 0 & \cdots & R_{n,x} & 0 \\ 0 & R_{1,y} & 0 & R_{2,y} & \cdots & 0 & R_{n,y} \\ R_{1,y} & R_{1,x} & R_{2,y} & R_{2,x} & \cdots & R_{n,y} & R_{n,x} \end{bmatrix}.$$

here $R_{i,x} = \frac{d}{dx}R_i$ and $R_{i,y} = \frac{d}{dy}R_i$. Using Equation 2.18, (2.20) and (2.21), the system of equations are obtained as

$$[\boldsymbol{K}]\{\boldsymbol{d}\} = \{\boldsymbol{F}\}, \tag{2.22}$$

where $\boldsymbol{K}$ and $\boldsymbol{F}$ are the global stiffness matrix and the global force vector, defined as

$$\boldsymbol{K} = \sum_{e=1}^{n} [\boldsymbol{L}_e]^T [\boldsymbol{K}_e][\boldsymbol{L}_e],$$

$$\text{where } \boldsymbol{K}_e = \int_{\Omega_e} [\boldsymbol{B}_e]^T [\boldsymbol{D}][\boldsymbol{B}_e] \ d\Omega_e.$$

$$\text{and } \boldsymbol{F} = \sum_{e=1}^{n} \left\{ [\boldsymbol{L}_e]^T \{\boldsymbol{F}_e^f\} + [\boldsymbol{L}_e]^T \{\boldsymbol{F}_e^h\} \right\}, \tag{2.23}$$

$$\text{where } \boldsymbol{F}_e = \int_{\Omega} [\boldsymbol{N}_e]^T \{\boldsymbol{f}\} \ d\Omega + \int_{\Gamma_N} [\boldsymbol{N}_e]^T \{\boldsymbol{h}\} \ d\Gamma_N.$$

where $\boldsymbol{K}_e$ and $\boldsymbol{F}_e$ are the element stiffness and element force entries of an element e. n is the number of elements in the design domain.

2.1.5   Evaluation of Stiffness Entries in Master Element

Element Stiffness matrix for an element e can be defined as

$$\boldsymbol{K}_e = \int_{\Omega_e} [B_e]^T [D][B_e] \quad d\Omega_e. \tag{2.24}$$

where,

$$\boldsymbol{B}_e = \begin{bmatrix} R_{1,x} & 0 & R_{2,x} & 0 & \cdots & R_{n,x} & 0 \\ 0 & R_{1,y} & 0 & R_{2,y} & \cdots & 0 & R_{n,y} \\ R_{1,y} & R_{1,x} & R_{2,y} & R_{2,x} & \cdots & R_{n,y} & R_{n,x} \end{bmatrix}$$

The physical coordinates and the shape functions are related as

$$\begin{aligned} x &= x_1 R_1(\xi, \eta) + x_2 R_2(\xi, \eta) + \cdots + x_n R_n(\xi, \eta), \\ y &= y_1 R_1(\xi, \eta) + y_2 R_2(\xi, \eta) + \cdots + y_n R_n(\xi, \eta). \end{aligned} \tag{2.25}$$

Applying the chain rule to calculate the derivatives of the shape functions as,

$$\frac{\partial R}{\partial x_i} = \frac{\partial R}{\partial \xi_j} \frac{\partial \xi_j}{\partial x_i}. \tag{2.26}$$

The derivatives of shape functions calculated in the parameter space are mapped to the master space $(\tilde{\xi}, \tilde{\eta})$. From Equation 2.25,

$$\frac{\partial R}{\partial \xi_j} = \frac{\partial R}{\partial \tilde{\xi}_k} \frac{\partial \tilde{\xi}_k}{\partial \xi_j}. \tag{2.27}$$

From Equation 2.25 and Equation 2.27, the jacobians needed to convert the integration from the physical space to the master element are devised as,

$$\boldsymbol{J}1 = \begin{bmatrix} \frac{\partial y}{\partial \eta} & \frac{-\partial y}{\partial \xi} \\ \frac{-\partial x}{\partial \eta} & \frac{\partial x}{\partial \xi} \end{bmatrix}, \boldsymbol{J}2 = \begin{bmatrix} \frac{\partial \eta}{\partial \tilde{\eta}} & 0 \\ 0 & \frac{\partial \xi}{\partial \tilde{\xi}} \end{bmatrix} \tag{2.28}$$

By using Equation 2.28, the derivatives of the shape functions can be found out by,

$$\begin{Bmatrix} R_{,x} \\ R_{,y} \end{Bmatrix} = \frac{1}{|\boldsymbol{J}1||\boldsymbol{J}2|}[\boldsymbol{J}1][\boldsymbol{J}2] \begin{Bmatrix} R_{,\tilde{\xi}} \\ R_{,\tilde{\eta}} \end{Bmatrix} \tag{2.29}$$

The equivalent stiffness matrix evaluation for an element e in the master element is done by using the following expression,

$$[\boldsymbol{K}_e] = \sum_{i=1}^{p_\xi} \sum_{j=1}^{p_\eta} [\boldsymbol{B}(\tilde{\xi}_i, \tilde{\eta}_j)]^T [\boldsymbol{D}][\boldsymbol{B}(\tilde{\xi}_i, \tilde{\eta}_j)]|\boldsymbol{J}1(\tilde{\xi}_i, \tilde{\eta}_j)|\boldsymbol{J}2(\tilde{\xi}_i, \tilde{\eta}_j)|. \tag{2.30}$$

where, p_ξ and p_η represents the total number of gauss points in the mater element in $\tilde{\xi}$ and $\tilde{\eta}$ directions.

2.2 Numerical examples

In this section, the developed finite element tool was used to solve some elastic 2D and 3D structures assuming small deformation and linear stress-strain relationship. The obtained results were again compared with the analytical solution to check the correctness of the developed code.

2.2.1 Bar with Axial Loading

Consider an isotropic rectangular bar having unit thickness, length 0.05 m and width 0.03 m, fixed at the left end, and external traction of 1000 MPa applied on the other end as shown in Figure 2.2. The material parameters of the bar are given in table 2.1.
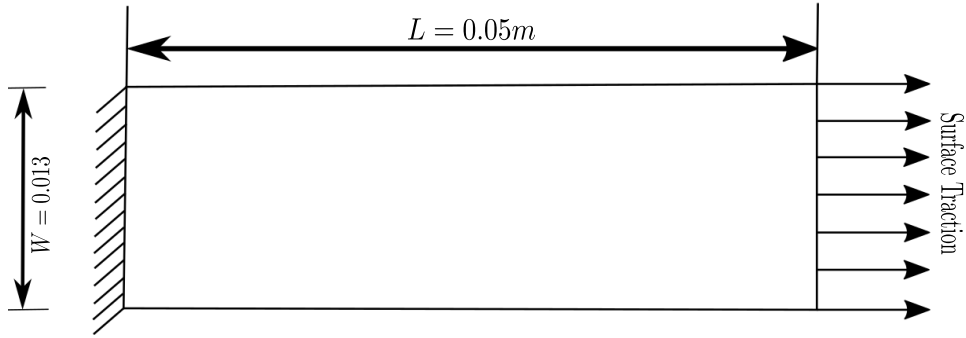
Figure 2.2: Description of the bar subjected to axial loading.
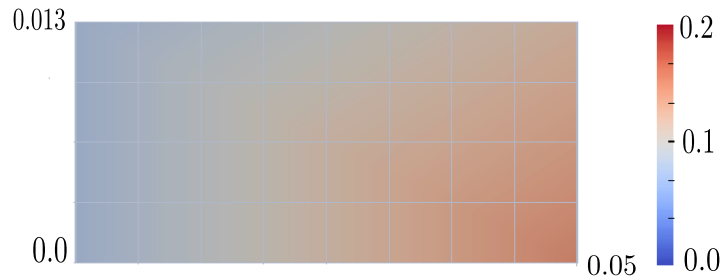
Figure 2.3: Displacement along x-direction (mm).

Table 2.1: Axial Bar Material Parameters.

Elastic Modulus(N/m^2)	Poison's ratio
100,000	0.25

The analytical solution for displacement of the bar at the free end is given by

$$u_{xl} = \frac{PL}{AE} \tag{2.31}$$
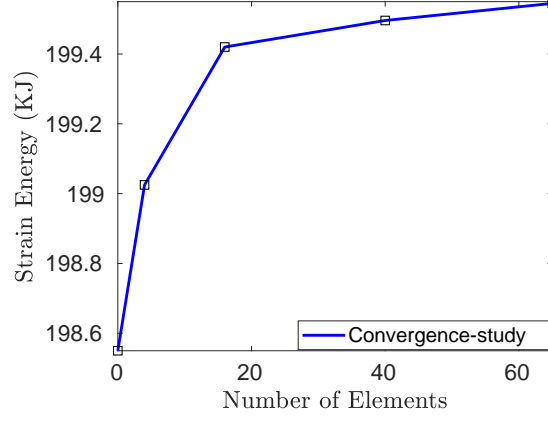
Figure 2.4: Convergence study.
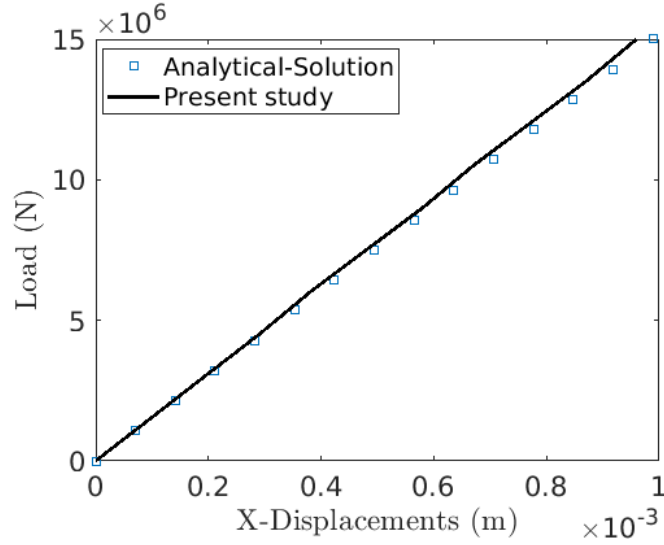
Figure 2.5: Simulated displacement response and comparison with analytical solution.

Where $P = t_x \times width$, t_x is the external traction and A is the cross-sectional area. The X-displacement at the right end is given by Equation 2.31. The x-displacements of the bar is shown in Figure 2.3. The convergence study is shown in Figure 2.4. The validation of the obtained solution is depicted in Figure 2.5

2.2.2 Plate with a hole

Consider an infinite plate with circular hole under constant in-plane tension (T = 1) at infinity as shown in Figure 2.6. The following problem can be solved by considering a quarter portion of the plate as shown in fig. 2.7 where R = 1m, radius of the hole and L = 10m, length of the finite quarter considered.
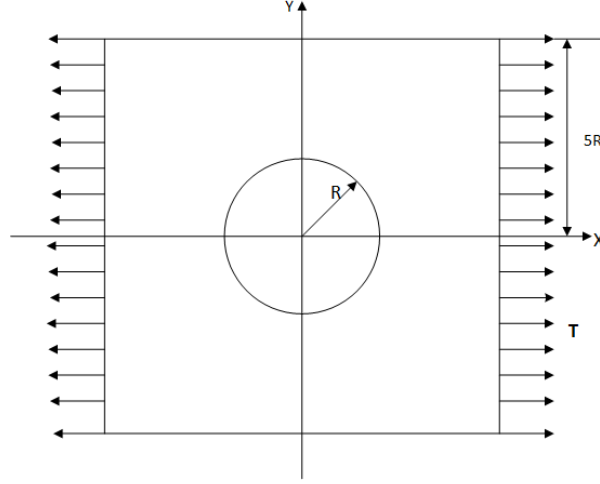
Figure 2.6: Description of the plate with a hole
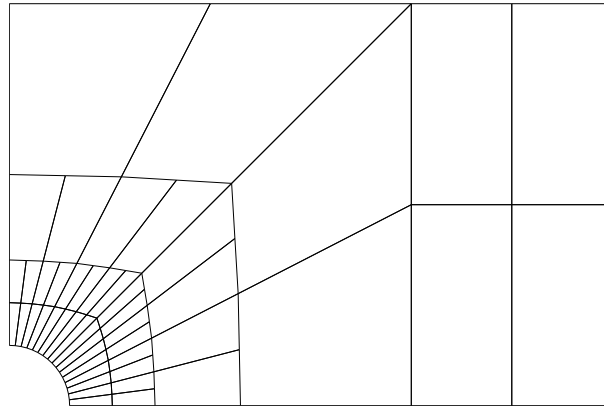
Figure 2.7: Portion of the plate analyzed

Parameter	Value
Young's Modulus E (MPa)	100,000
Poisson's ratio μ	0.3

Table 2.2: Plate with a hole material parameters

Results

The material parameters of the plate are given in table 2.2. The mesh in Figure 2.7 is analyzed and refined till convergence is achieved. The displacements obtained are

26

compared with the analytical solution obtained at r=R. Figure 2.8 and Figure 2.9 shows the convergence and validation of the problem respectively.
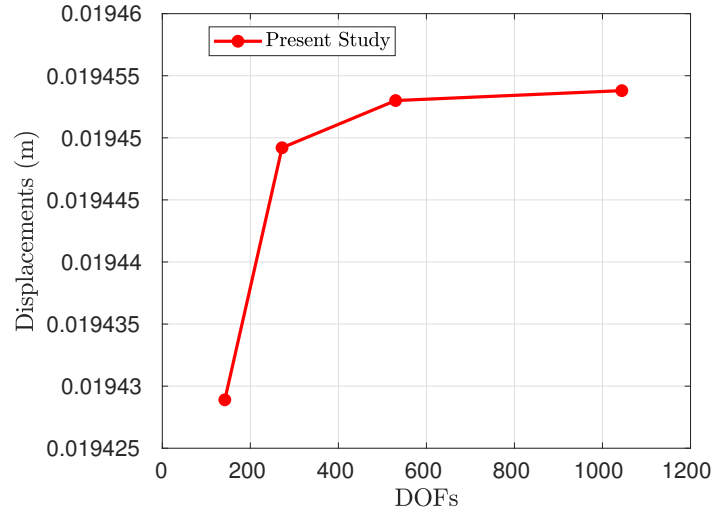
Figure 2.8: Convergence Study
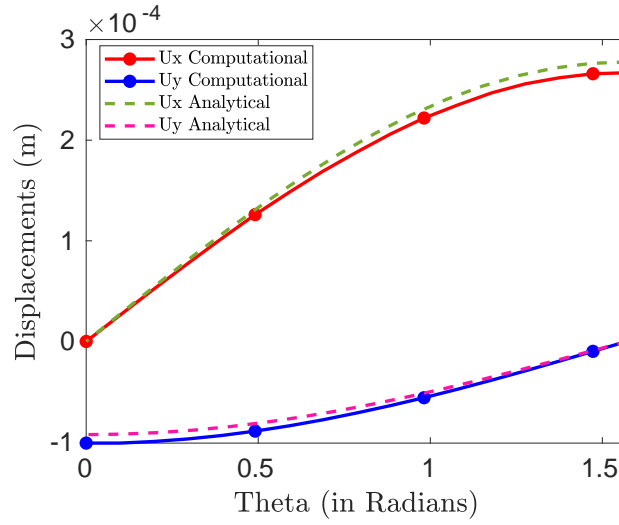
Figure 2.9: Validation of the solution

Obtained result was validated through the analytical solution for displacement of the plate with a hole for unit tension is given by,

$$u_x(r,\theta) = \frac{R}{8\mu}[\frac{r}{R}(k+1)cos\theta + \frac{2R}{r}((1+k)cos\theta + cos3\theta) - \frac{2R^3}{r^3}cos3\theta] \qquad (2.32)$$

$$u_y(r,\theta) = \frac{R}{8\mu}[\frac{r}{R}(k-3)sin\theta + \frac{2R}{r}((1-k)sin\theta + sin3\theta) - \frac{2R^3}{r^3}sin3\theta] \qquad (2.33)$$

Where,

$$\mu = \frac{E}{2(1+\mu)}nt \qquad (2.34)$$

$$k = \frac{3-\mu}{1+\mu} \qquad (2.35)$$

2.2.3   Elastic Beam

A 3D elastic beam having length 0.1 m, height 0.01 m and thickness 0.0015 m as shown in Figure 2.10 os considered for analysis. The beam is under a transverse load at the right hand side cross-section and fixed at the left hand side section. The maximum load acting is 16.67 MN and loading/unlaoding cycle is as shown in Figure 2.11.
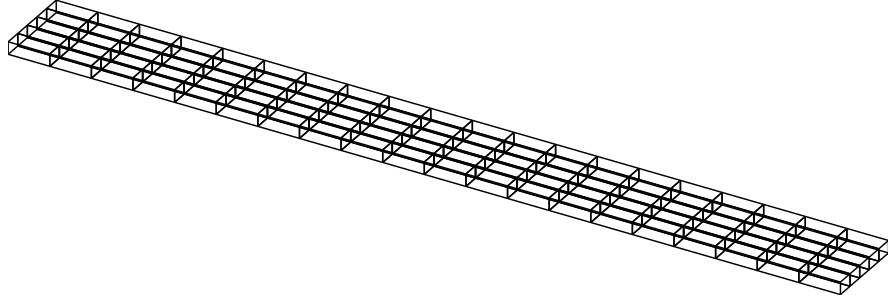
Figure 2.10: 3D Beam

The material parameters used for the FE analysis are enisted in table 2.3

Table 2.3: Elastic Beam material parameters

Parameter	Value
Young's Modulus	72 GPa
Poisson's ratio μ	0.42

Results

FE computation is done till convergence is achieved as shwon in Figure 2.15.

Again mesh is refined as per the stress concentration with two different coding procedure. First, the mesh is manually refined for stress concentration and second, using adaptive refined technique, in which it is refined and coarsened at each set time step of loading on the basis of stress concentration development in the cross-section. Both the
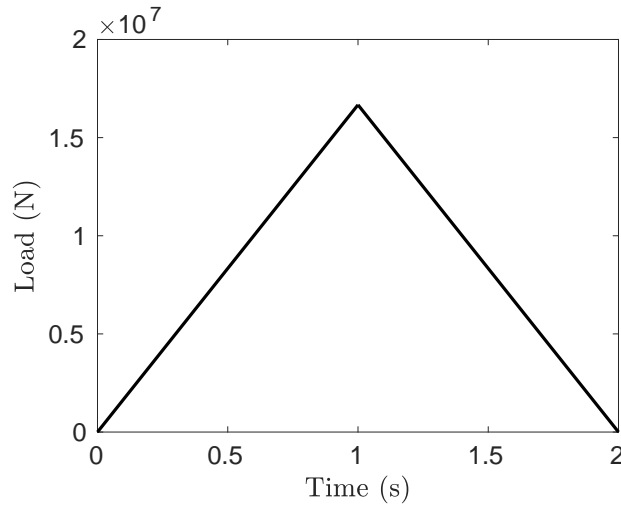
Figure 2.11: Load vs time graph.

meshes are shown in Figure 2.13. The load-displacement for each meshes is shown in Figure 2.14. and as we can see, as the degrees of freedom increases, load-displacement plot starts to converge. Figure 2.15 (a) shwos the convergence study for the deflection at the tip.

Figure 2.12: initial mesh

Figure 2.13: (a)Refined at maximum stress concentration and (b) using adaptive refined technique.
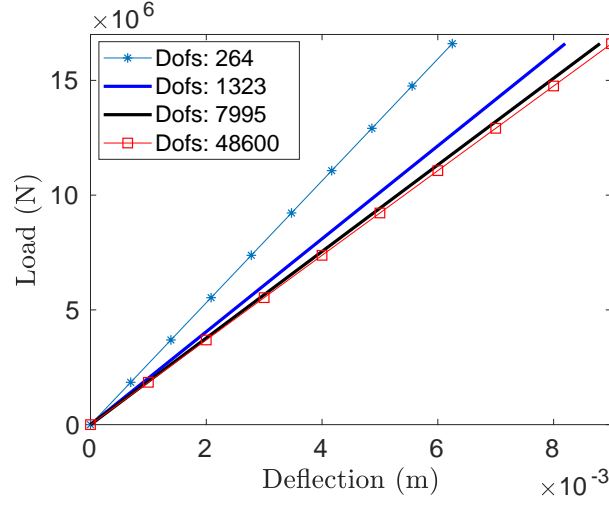
Figure 2.14: Mesh convergence study.
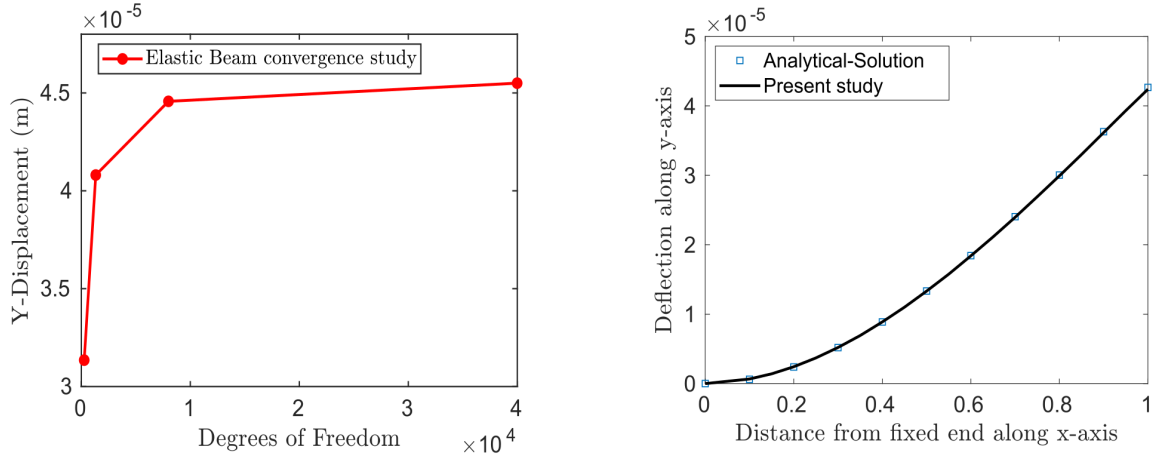
Figure 2.15: (a) Convergence study (b) simulated tip deflection and comparison with analytical result

The analytical solution for displacement of the Beam for the transverse load acting at free end is given by the Euler-Bernouli equation given as below,

$$EI\frac{d^2y}{dx^2} = -M \tag{2.36}$$

Integrating Equation 2.36 and applying valid boundary conditions, we can get the deflection of the beam as,

$$y = \frac{p}{EI}[-2l^3 + 3l^2 - x^3] \tag{2.37}$$

Figure 2.15 (b) shows the validation of the elastic beam problem using analytical solution.

2.2.4 Elastic Spring

A helical spring is considered having one turn as shown in Figure 2.16 . The spring has a mean coil radius of 0.02 m and cross-section wire diameter of 0.005 m. The spring has an Elastic Modulus of 70 GPa and the poison ratio of 0.30. For analyzing the helical spring using the finite Element method, spring mesh were generated using abaqus and then the mesh information generated as 'inp-file' is fed to the FE code. Figure 2.17 illustrates the convergence study of the problem.
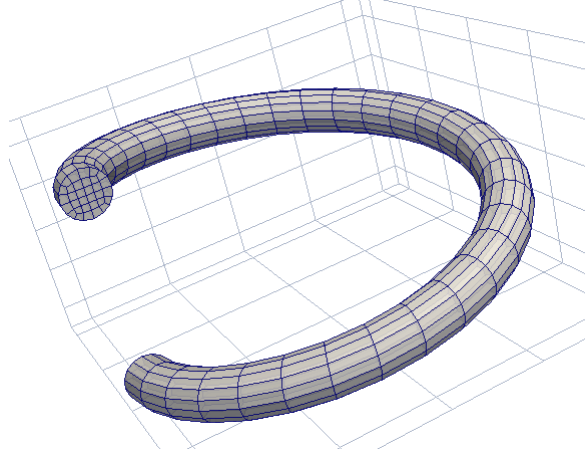
Figure 2.16: Schematic representation of helical spring.
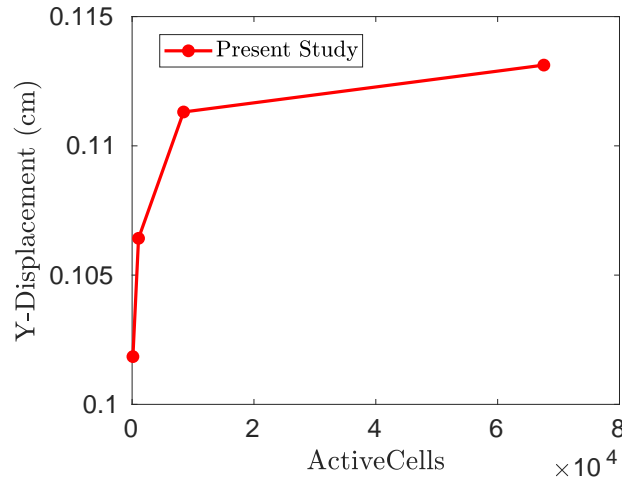
Figure 2.17: Convergence study.

Results

FE analysis of the problem is done till convergence is achieved. The convergence analysis is shown in Figure 2.17. For this, the displacement of the point at the free end is considered.

The spring mesh is again refined adaptively, Figure 2.18, instead of refining globally and results obtained were compared against the initial result as shown in Figure 2.19 which shows adaptive refined technique is nearly able to simulate the elastic behaviour.
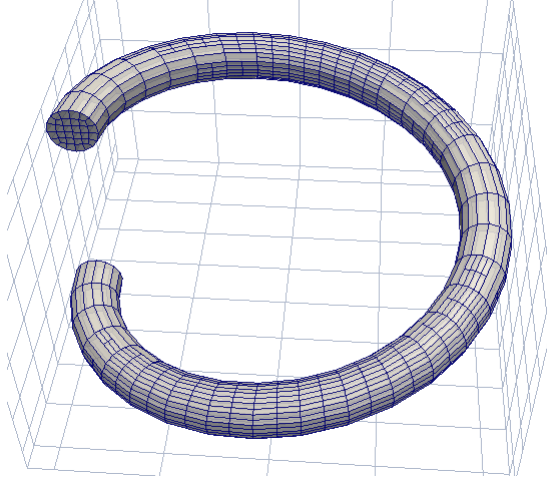
Figure 2.18: Adaptively refined spring mesh.
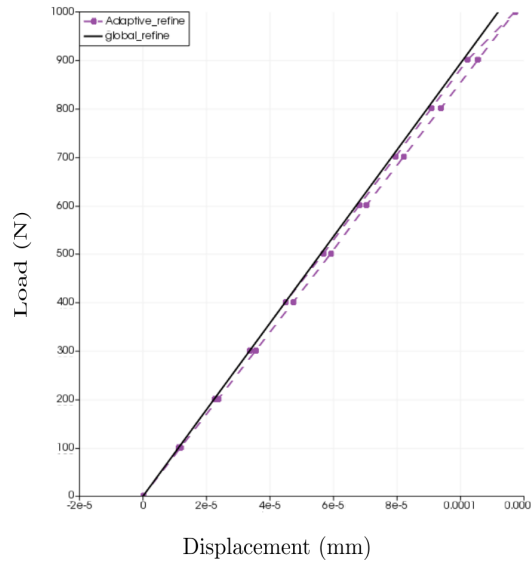
Figure 2.19: Comparison between global and adaptive mesh FE simulation.

The load-displacement relationship shown in Figure 2.19 is plotted against the complete loading and unloading of the spring. The globally refined mesh took around 10 hours to run while the adaptively refined mesh took around five and a half hours to completely run the code. As we can see, the adaptively refined mesh gives almost the similar result as the globally refined mesh, thus it is preferable to use the adaptive meshing for such elastic problems.

Analytical solution

The analytical solution for deflection at the free end of an elastic beam is given as below:

$$\delta = \frac{64WR^3}{Gd^4} \tag{2.38}$$

Where, W is the applied load, R is mean coil radius, G is the modulus of rigidity and d is wire diameter. The result obtained through converged mesh and adaptive mesh were compared against the given analytical solution shown in Figure 2.20.
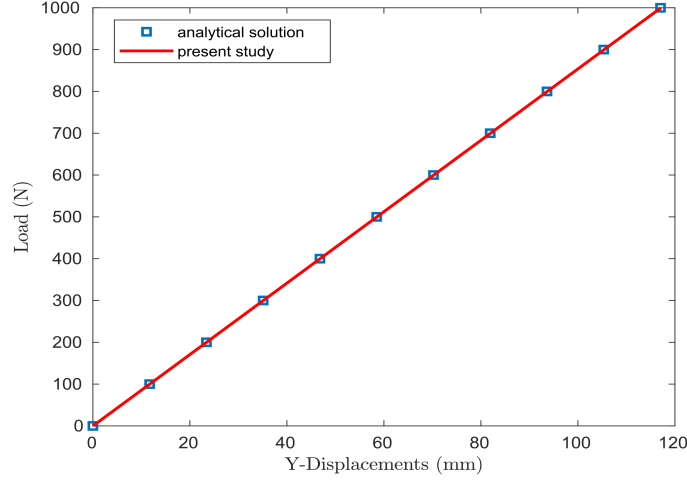
Figure 2.20: Simulated tip displacement in y-direction and comparison with analytical result.

2.2.5 Elastic Torque Tube

Consider a cylindrical tube as shown in Figure 2.21. the inner and outer radius of the tube is 2.5 mm, and 3.17 mm respectively and the length is 82 m. The tube is fully fixed at the left end and angular (rotation) boundary condition is applied at the other end. Torque tube is loaded in simple shear (torsion) with maximum value of applied rotation is 1 radian(57.3 deg).
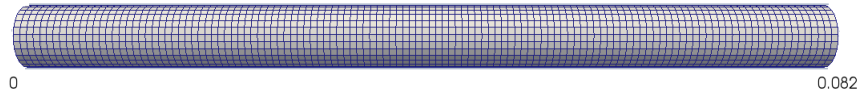
Figure 2.21: Schematic representation torque tube mesh

The initial mesh has only 200 elements and only one element is used in the radial direction, since the tube is very thin. Again, mesh is refined till convergence is achieved. Convergence starts above 5000 elements meshing. Obtained results were validated by

using torque and theta relationship of analytical study. Convergence and validtion study has been shown in Figure 2.22.
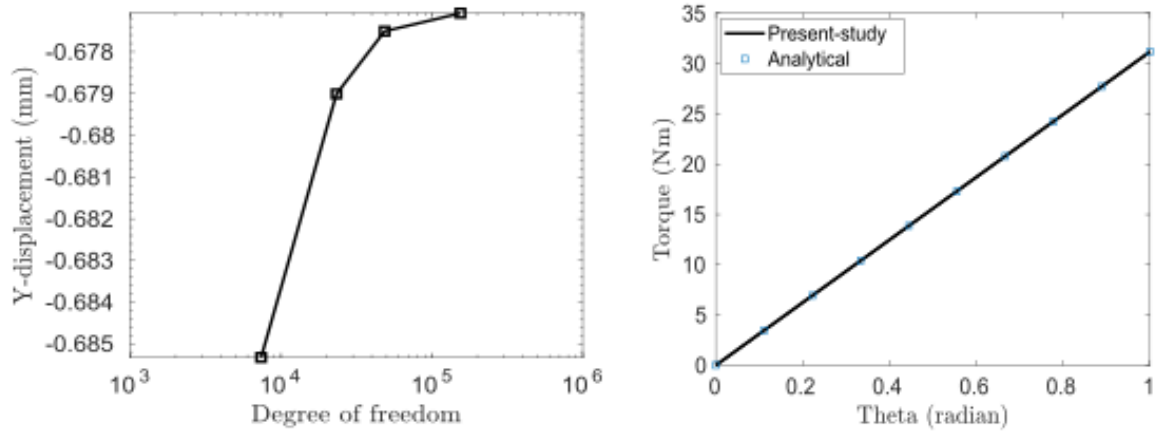
Figure 2.22: (a) Convergence study and (b) validation study using torque-theta plot at free end.

Chapter 3

Constitutive model of shape memory alloy and nonlinear finite element formulation

In this chapter, the thermodynamic based constitutive model is presented for a polycrystalline shape memory alloys as proposed by [2]. The stress-strain-temperature state is determined by following the procedure of classical plasticity by considering internal state variables. Gibbs free energy function is written as the thermodynamic potential, because thermo-mechanical loading path is defined by the stress-temperature space. First, the detailed derivation of the constitutive model is presented followed by its numerical implementation in a finite element framework as given by [24].

3.1   Constitutive Modeling of SMAs

The Gibbs free energy (G) function is depicted in terms of stress $(\boldsymbol{\sigma})$, temperature (T) and other internal state parameters like martensitic volume fraction (ξ) and transformation strain $(\boldsymbol{\varepsilon_t})$. The explicit form of Gibbs free energy is taken as

$$G(\boldsymbol{\sigma}, T, \xi, \boldsymbol{\varepsilon}^t) = -\frac{1}{2\rho}\boldsymbol{\sigma} : \boldsymbol{S} : \boldsymbol{\sigma} - \frac{1}{\rho}\boldsymbol{\sigma} : [\boldsymbol{\alpha}(T - T_0) + \boldsymbol{\varepsilon}^t] + c[(T - T_0) - T\ln(\frac{T}{T_0})] - s_0 T + u_0 + \frac{1}{\rho}f(\xi)$$
(3.1)

where T_0 is a reference temperature. The material parameters $\boldsymbol{S}$ is the the fourth-order effective compliance tensor, $\boldsymbol{\alpha}$ is the the second-order effective thermal expansion tensor, and c is the effective specific heat, s_0 is the effective specific entropy at the reference state, and u_0 is the effective specific internal energy at the reference state. The transformation hardening function is denoted $f(\xi)$.

The expression for the Gibbs free energy is based on the concept of a linear thermoelastic material by considering a combination two such materials, viz. austenite $(*^A)$ and martensite $(*^M)$ into one through martensitic volume fraction (ξ). Thus, the effective

material properties can be determined by the following expressions:

$$\boldsymbol{S} := \boldsymbol{S}^A + \xi(\boldsymbol{S}^M - \boldsymbol{S}^A)$$
$$\boldsymbol{\alpha} := \boldsymbol{\alpha}^A + \xi(\boldsymbol{\alpha}^M - \boldsymbol{\alpha}^A)$$
$$c := c^A + \xi(c^M - c^A)$$
$$s_0 := s_0{}^A + \xi(s_0{}^M - s_0{}^A)$$
$$u_0 := u_0{}^A + \xi(u_0{}^M - u_0{}^A)$$

The Gibbs free energy is related to the internal energy, u, by the Legendre transformation:

$$u(\boldsymbol{\sigma}, s, \xi, \boldsymbol{\varepsilon}^t) = G + Ts + \frac{1}{\rho}\boldsymbol{\sigma} : \boldsymbol{\varepsilon} \tag{3.2}$$

where, $\boldsymbol{\varepsilon}$ is the total strain tensor. From the first and second law of thermodynamics, and by substituting G and u, thermodynamic constraints on state of the system results in the following constitutive relations:

$$\boldsymbol{\varepsilon} = -\rho\frac{\partial G}{\partial \boldsymbol{\sigma}} = \boldsymbol{S} : \boldsymbol{\sigma} + \boldsymbol{\alpha}(T - T_0) + \boldsymbol{\varepsilon}^t \tag{3.3}$$

$$s = -\frac{\partial G}{\partial T} = \frac{1}{\rho}\boldsymbol{\sigma} : \boldsymbol{\alpha} + c\ln(\frac{T}{T_0}) + s_0 \tag{3.4}$$

The Gibbs free energy in Equation 3.1 is substituted in Clausis-Planck inequality, yielding

$$(-\rho\frac{\partial G}{\partial \boldsymbol{\varepsilon}^t}) : \dot{\boldsymbol{\varepsilon}}^t + (-\rho\frac{\partial G}{\partial \xi})\dot{\xi} \geq 0 \tag{3.5}$$

$$\boldsymbol{\sigma} : \dot{\boldsymbol{\varepsilon}}^t + (-\rho\frac{\partial G}{\partial \xi})\dot{\xi} \geq 0 \tag{3.6}$$

To simplify the analysis for the case of phase transformation without reorientation, it is taken that any alteration of the current state of the system is only possible by a change in the martensitic volume fraction and that any other internal state variable evolves with it . Based on this criterion, the following relation can be postulated to relate the evolution of transformation strain tensor to the evolution of the martensitic volume fraction in rate form:

$$\dot{\boldsymbol{\varepsilon}}^t = \boldsymbol{\Lambda}\dot{\xi} \tag{3.7}$$

where $\boldsymbol{\Lambda}$ is the transformation tensor which determines the transformation strain considering the flow direction and is assumed to have the following form:

$$\boldsymbol{\Lambda} = \begin{cases} \frac{3}{2}H\frac{\boldsymbol{\sigma}'}{\bar{\sigma}} & ; & \dot{\xi} > 0 \\ H\frac{\boldsymbol{\varepsilon}^{t-r}}{\bar{\varepsilon}^{t-r}} & ; & \dot{\xi} < 0 \end{cases} \tag{3.8}$$

where, H denotes the maximum uniaxial transformation strain, ε^{t-r} is the transformation strain at the reversal of phase transformation.

$$\sigma' = \sqrt{\frac{3}{2}}\|\sigma'\|, \sigma' = \sigma - \frac{1}{3}(tr\sigma)1, \bar{\varepsilon}^{t-r} = \sqrt{\frac{2}{3}}\|\varepsilon^{t-r}\| \tag{3.9}$$

where $\| * \|^2 = (* : *)$ is the inner product of the enclosed quantity. Here transformation strain rate, $\dot{\varepsilon}^t$, is only a part of the total inelastic strain rate, $\dot{\varepsilon}^{in}$.

Using Equation 3.7 the total dissipation rate takes the following form

$$(\sigma : \Lambda - \rho\frac{\partial G}{\partial \xi})\dot{\xi} = \pi\dot{\xi} \geq 0 \tag{3.10}$$

where π is the thermodynamic force conjugate to ξ, which is obtained after substitution from Equation 3.1 as

$$\pi(\sigma, T, \xi) = \sigma : \Lambda - \frac{1}{2}\sigma : \Delta S : \sigma + \sigma : \Delta\alpha(T - T_0) + \rho\Delta c[(T - T_0) - T\ln(\frac{T}{T_0})] + \rho\Delta s_0 T - \rho\Delta u_0 - \frac{\partial f}{d\xi} \tag{3.11}$$

The terms that are defined with the prefix Δ in Equation 3.11 indicate the difference of a quantity between the martensitic and austenitic phases, and they are given by

$$\Delta S = S^M - S^A, \Delta\alpha = \alpha^M - \alpha^A, \Delta c = c^M - c^A, \Delta s_0 = s_0{}^M - s_0{}^A, \Delta u_0 = u_0{}^M - u_0{}^A \tag{3.12}$$

The transformation function (ϕ) is defined in terms of the thermodynamic force:

$$\phi := \begin{cases} \pi - Y^*, & \dot{\xi} > 0 \\ -\pi - Y^*, & \dot{\xi} < 0 \end{cases} \tag{3.13}$$

where Y^* measures the internal dissipation due to phase transformation. Similar to the maximum plastic dissipation principle, constraints on the evolution of the martensitic volume fraction are determined from a maximum transformation dissipation theory, are expressed in terms of the Kuhn-Tucker inequalities as

$$\begin{aligned} \dot{\xi} \geq 0, \quad \phi(\sigma, T, \xi) \leq 0, \quad \phi\dot{\xi} = 0 \\ \dot{\xi} \leq 0, \quad \phi(\sigma, T, \xi) \leq 0, \quad \phi\dot{\xi} = 0 \end{aligned} \tag{3.14}$$

Here, the transformation function $\phi(\sigma, T, \xi)$ denotes the transformation surface that defines the elastic domain. The inequality constraints on $\phi(\sigma, T, \xi)$ is called the transformation (consistency) condition and viewed as a constraint on the state variables admissibility. Along any loading path, all the relations should hold simultaneously. For $\phi < 0$ in Equation 3.14, $\dot{\xi} = 0$ and elastic response is obtained. On the other hand, the forward-phase transformation (austenite → martensite) is characterized by $\phi = 0$ and $\dot{\xi} > 0$ while the reverse-phase transformation (martensite → austenite) is characterized $\phi = 0$ and $\dot{\xi} < 0$.

The hardening function, $f(\xi)$, accounts for the transformation-induced strain hardening in the SMA and is given by following hardening model.

Polynomial Model:

$$f(\xi) = \begin{cases} \frac{1}{2}\rho b^M \xi^2 + (\mu_1 + \mu_2)\xi, & \dot{\xi} > 0 \\ \frac{1}{2}\rho b^A \xi^2 + (\mu_1 - \mu_2)\xi & \dot{\xi} < 0 \end{cases} \tag{3.15}$$

where, the material parameters are:

$$\begin{aligned} \rho\Delta s_0 &= -C_A H_{\max} \\ \rho\Delta u_0 &= \tfrac{1}{2}\rho\Delta s_0(M_s + A_f) \\ \rho b^A &= -\rho\Delta s_0(A_f - A_s) \\ \rho b^M &= -\rho\Delta s_0(M_s - M_f) \\ \mu_1 &= \tfrac{1}{2}\rho\Delta s_0(M_s + A_f) - \rho\Delta u_0 \\ \mu_2 &= \tfrac{1}{4}(\rho b^A - \rho b^M) \\ Y &= -\tfrac{1}{2}\rho\Delta s_0(A_f - M_s) + \tfrac{1}{4}\rho\Delta s_0(M_s - M_f - A_f + A_s) \end{aligned}$$

Exponential Model:

$$f(\xi) = \begin{cases} \frac{\rho\Delta s_0}{a_e^M}\left[(1-\xi)\ln(1-\xi) - \xi\right] + (\mu_1^e + \mu_2^e)\xi, & \dot{\xi} > 0 \\ \frac{\rho\Delta s_0}{a_e^M}\left[\ln(\xi) - 1\right] + (\mu_1^e + \mu_2^e)\xi, & \dot{\xi} < 0 \end{cases} \tag{3.16}$$

where, the material parameters are:

$$\begin{aligned} \rho\Delta s_0 &= -C_A H_{\max} \\ \rho\Delta u_0 &= \tfrac{1}{2}\rho\Delta s_0(M_s + A_f) \\ a_e^A &= -\frac{\ln(0.01)}{(A_s - A_f)} \\ a_e^M &= \frac{\ln(0.01)}{(M_s - M_f)} \\ \mu_1^e &= \tfrac{1}{2}\rho\Delta s_0(M_s + A_s + \tfrac{2}{a_e^M}) - \rho\Delta u_0 \\ \mu_2^e &= \tfrac{1}{2}\rho\Delta s_0(\tfrac{1}{a_e^M} - \tfrac{1}{a_e^A}) \\ Y &= \tfrac{1}{2}\rho\Delta s_0\left(M_s + \tfrac{1}{a_e^M} + \tfrac{1}{a_e^A} - A_s\right) \end{aligned}$$

Cosine Model:

$$f(\xi) = \begin{cases} \int\limits_0^\xi -\frac{\rho\Delta s_0}{a_c^M}\left[\pi - \cos^{-1}(2\xi - 1)\right]d\xi + (\mu_1^c + \mu_2^c)\xi, & \dot{\xi} > 0 \\ \int\limits_0^\xi -\frac{\rho\Delta s_0}{a_c^A}\left[\pi - \cos^{-1}(2\xi - 1)\right]d\xi + (\mu_1^c - \mu_2^c)\xi, & \dot{\xi} < 0 \end{cases} \tag{3.17}$$

where, the material parameters are:

$$\rho \Delta s_0 = -C_A H_{\max}$$
$$\rho \Delta u_0 = \tfrac{1}{2}\rho \Delta s_0 (M_s + A_f)$$
$$a_c^A = -\frac{\pi}{(A_s - A_f)}$$
$$a_c^M = \frac{\pi}{(M_s - M_f)}$$
$$\mu_1^c = \tfrac{1}{2}\rho \Delta s_0 (M_s + A_f) - \rho \Delta u_0$$
$$\mu_2^c = \tfrac{\pi}{2}\rho \Delta s_0 \left(\tfrac{1}{a_c^M} - \tfrac{1}{a_c^A}\right)$$
$$Y = \frac{\rho \Delta s_0}{2}(M_f - A_s)$$

where, transformation strain hardening material constants are denoted by ρb^M, ρb^A, μ_1, μ_2. The trigonometric, logarithmic, or any other functions can also be used to express hardening function ($f(\xi)$) in place of of polynomial function to accommodate other constitutive models viz. [18], [19].

3.1.1 Continuum Tangent Moduli Tensors

In an incremental displacement-based finite element framework, the increment of the stress tensor ($d\boldsymbol{\sigma}$) is obtained through the implementation of the incremental SMA constitutive model for given increments of strain ($d\boldsymbol{\varepsilon}$) and temperature ($dT$). The SMA constitutive model can be written in an incremental form as follows:

$$d\boldsymbol{\sigma} = \boldsymbol{L} : d\boldsymbol{\varepsilon} + \boldsymbol{\Theta} dT \tag{3.18}$$

where $\boldsymbol{L}$ is the tangent stiffness tensor and $\boldsymbol{\Theta}$ is the tangent thermal moduli tensor. These two tensors are needed for the execution of the global finite element analysis (FEA). In order to derive $\boldsymbol{L}$ and $\boldsymbol{\Theta}$, the constitutive relation is written in differential form and the transformation strain flow rule is substituted to get

$$d\boldsymbol{\sigma} = \boldsymbol{S}^{-1} : \{d\boldsymbol{\varepsilon} - \boldsymbol{\alpha} dT - [\Delta \boldsymbol{S} : \boldsymbol{\sigma} + \Delta \boldsymbol{\alpha}(T - T_0) + \boldsymbol{\Lambda}] d\xi\} \tag{3.19}$$

The above equation further reduces to

$$d\boldsymbol{\sigma} = \boldsymbol{S}^{-1} : \left(d\boldsymbol{\varepsilon} - \boldsymbol{\alpha} dT - d\xi \begin{cases} \frac{\partial \phi}{\partial \boldsymbol{\sigma}}, & \dot{\xi} > 0 \\ -\frac{\partial \phi}{\partial \boldsymbol{\sigma}}, & \dot{\xi} < 0 \end{cases} \right) \tag{3.20}$$

On the other hand, the differentiation of the transformation function (consistency condition) results in

$$d\phi = \frac{\partial \phi}{\partial \boldsymbol{\sigma}} : \boldsymbol{\sigma} + \frac{\partial \phi}{\partial T} : T + \frac{\partial \phi}{\partial \xi} : \xi = 0 \tag{3.21}$$

For forward transformation, an expression for the differential of the martensite volume fraction $d\xi$, is obtained by substituting $d\boldsymbol{\sigma}$ from the above two equations

$$d\xi = \frac{\partial_{\boldsymbol{\sigma}}\phi : \boldsymbol{S}^{-1} : d\boldsymbol{\varepsilon} + (\partial_T\phi - \partial_{\boldsymbol{\sigma}}\phi : \boldsymbol{S}^{-1} : \boldsymbol{\alpha})dT}{\partial_{\boldsymbol{\sigma}}\phi : \boldsymbol{S}^{-1} : \partial_{\boldsymbol{\sigma}}\phi - \partial_\xi\phi} \tag{3.22}$$

From Equation 3.22 we can obtain the relationship between the stress and strain and temperature increments.

$$d\boldsymbol{\sigma} = [\boldsymbol{S}^{-1} - \frac{\boldsymbol{S}^{-1} : \partial_{\boldsymbol{\sigma}}\phi \otimes \boldsymbol{S}^{-1} : \partial_{\boldsymbol{\sigma}}\phi}{\partial_{\boldsymbol{\sigma}}\phi : \boldsymbol{S}^{-1} : \partial_{\boldsymbol{\sigma}}\phi - \partial_\xi\phi}] : d\boldsymbol{\varepsilon} + \boldsymbol{S}^{-1} : [\partial_{\boldsymbol{\sigma}}\phi(\frac{\partial_{\boldsymbol{\sigma}}\phi : \boldsymbol{S}^{-1} : \boldsymbol{\alpha} - \partial_T\phi}{\partial_{\boldsymbol{\sigma}}\phi : \boldsymbol{S}^{-1} : \partial_{\boldsymbol{\sigma}}\phi - \partial_\xi\phi}) - \boldsymbol{\alpha}]dT \tag{3.23}$$

The tangent stiffness tensor $\boldsymbol{L}$, and tangent thermal moduli tensor, $\boldsymbol{\Theta}$ are then given, after some simplification of Equation 3.23

$$\begin{aligned}
\boldsymbol{L} &= \boldsymbol{S}^{-1} - \boldsymbol{A} \otimes \boldsymbol{A} \\
\boldsymbol{\Theta} &= -\boldsymbol{L} : \boldsymbol{\alpha} - \frac{\partial_T\phi}{a}\boldsymbol{A} \\
&\text{where,} \\
a &:= \sqrt{\partial_{\boldsymbol{\sigma}}\phi : \boldsymbol{S}^{-1} : \partial_{\boldsymbol{\sigma}}\phi - \partial_\xi\phi} \\
\boldsymbol{A} &:= \frac{\boldsymbol{S}^{-1}:\partial_{\boldsymbol{\sigma}}\phi}{\sqrt{\partial_{\boldsymbol{\sigma}}\phi:\boldsymbol{S}^{-1}:\partial_{\boldsymbol{\sigma}}\phi-\partial_\xi\phi}} = \frac{\boldsymbol{S}^{-1}:\partial_{\boldsymbol{\sigma}}\phi}{a}
\end{aligned} \tag{3.24}$$

Similarly, for the reverse transformation the expression for $\boldsymbol{L}$ and $\boldsymbol{\Theta}$ is obtained,

$$d\xi = -\frac{\partial_{\boldsymbol{\sigma}}\phi : \boldsymbol{S}^{-1} : d\boldsymbol{\varepsilon} + (\partial_T\phi - \partial_{\boldsymbol{\sigma}}\phi : \boldsymbol{S}^{-1} : \boldsymbol{\alpha})dT}{\partial_{\boldsymbol{\sigma}}\phi : \boldsymbol{S}^{-1} : \partial_{\boldsymbol{\sigma}}\phi + \partial_\xi\phi} \tag{3.25}$$

$$\begin{aligned}
\boldsymbol{L} &= \boldsymbol{S}^{-1} - \boldsymbol{B} \otimes \boldsymbol{B} \\
\boldsymbol{\Theta} &= -L : \boldsymbol{\alpha} - \frac{\partial_T\phi}{a}\boldsymbol{B} \\
&\text{where,} \\
b &:= \sqrt{\partial_{\boldsymbol{\sigma}}\phi : \boldsymbol{S}^{-1} : \partial_{\boldsymbol{\sigma}}\phi + \partial_\xi\phi} \\
\boldsymbol{B} &:= \frac{\boldsymbol{S}^{-1}:\partial_{\boldsymbol{\sigma}}\phi}{\sqrt{\partial_{\boldsymbol{\sigma}}\phi:\boldsymbol{S}^{-1}:\partial_{\boldsymbol{\sigma}}\phi+\partial_\xi\phi}} = \frac{\boldsymbol{S}^{-1}:\partial_{\boldsymbol{\sigma}}\phi}{b}
\end{aligned} \tag{3.26}$$

3.2 Return Mapping Algorithm

Equation 3.3 and (3.7) governs the phase transformation phenomenon and constrained by Kuhn-Tucker condition as given by Equation 3.14. It is considered that the strain and temperature history $\boldsymbol{\varepsilon}^t$ and $T(t)$ is known for time interval $t \in [0, t^*]$, as well as the initial conditions for $\boldsymbol{\varepsilon}^t$ and ξ at $t = 0$. The evolution equation for relating the transformation strain ($\boldsymbol{\varepsilon}^t$) and martensitic volume fraction (ξ) are discretized using the generalized trapezoidal rule, given as

$$\boldsymbol{\varepsilon}_{n+1}^t = \boldsymbol{\varepsilon}_n^t + (\xi_{n+1} - \xi_n)[(1 - \beta)\boldsymbol{\Lambda}_n + \beta\boldsymbol{\Lambda}_{n+1}] \tag{3.27}$$

The parameter β ranges from $[0, 1]$ and subscript $(*)_n$ and $(*)_{n+1}$ signifies the function evaluations at time t_n and t_{n+1} respectively, where time increment $\Delta t = t_{n+1} - t_n$. For different values of β, various difference operators can be obtained. Two such values of β can be chosen which together demonstrate all the characteristics of this family of integration rules. Implicit (backward) Euler integration rule is obtained by $\beta = 1$. This implicit algorithm is implemented for the set of governing equations and Kuhn-Tucker conditions, as given by Equation 3.3, (3.7), and (3.14). Similarly, for $\beta = 0$ explicit (forward) integration rule is obtained. The return mapping algorithm divides this problem in a set of non-linear algebraic equations in an additive split. This requires multiple iterations to obtain a solution containing the transformation behavior.

3.2.1 Thermoelastic Prediction and Transformation Correction Return Mapping

The thermoelastic predictor problem is considered as a case when increment of the transformation strain is zero.

$$
\begin{aligned}
\dot{\boldsymbol{\varepsilon}} &= \dot{\boldsymbol{\varepsilon}}(t) \\
\dot{T} &= \dot{T}(t) \\
\dot{\boldsymbol{\varepsilon}}^t &= 0
\end{aligned}
\tag{3.28}
$$

The transformation corrector problem that restores the consistency condition if the predicted thermoelastic state goes outside the transformation surface ($\phi > 0$) is given by

$$
\begin{aligned}
\dot{\boldsymbol{\varepsilon}} &= 0 \\
\dot{T} &= 0 \\
\dot{\boldsymbol{\varepsilon}}^t &= \boldsymbol{\Lambda} \dot{\xi}
\end{aligned}
\tag{3.29}
$$

with the initial conditions is given by the solution of the elastic predictor problem, and the increment $\dot{\xi}$ is to be found by satisfying the transformation consistency condition. It is important to note that the history of the total strain tensor, $\boldsymbol{\varepsilon}(t)$, and temperature, $T(t)$, are given, the transformation function during the transformation correction will depend on the changes in $\boldsymbol{\sigma}$ and ξ. Since $d\boldsymbol{\varepsilon}$ and dT are zero during transformation correction Equation 3.20 results in

$$
\frac{d\boldsymbol{\sigma}}{d\xi} = \begin{cases} -\boldsymbol{S}^{-1} : \partial_{\boldsymbol{\sigma}}\phi, & \dot{\xi} > 0 \\ \boldsymbol{S}^{-1} : \partial_{\boldsymbol{\sigma}}\phi, & \dot{\xi} < 0 \end{cases}
\tag{3.30}
$$

The evolution of stress state starts towards the transformation surface at a trial thermoelastic state as inputted by the elastic predictor step and follows the steepest descent path with respect to the transformation surface, ϕ. Transformation consistency is enforced by determining the intersection of the stress evolution curve with the boundary of the transformation function (yield surface). By, differentiating ϕ with respect to ξ, recalling that temperature (T) is kept constant during transformation correction, and using the

expression for $\frac{d\boldsymbol{\sigma}}{d\xi}$ in Equation 3.30,

$$
\begin{aligned}
\frac{d}{d\xi}\phi(\boldsymbol{\sigma}, T|_{fixed}, \xi) &= \partial_{\boldsymbol{\sigma}}\phi : \frac{d\boldsymbol{\sigma}}{d\xi} + \partial_{\xi}\phi \\
&= \begin{cases} -\partial_{\boldsymbol{\sigma}}\phi : \boldsymbol{S}^{-1} : \partial_{\boldsymbol{\sigma}}\phi + \partial_{\xi}\phi, & \dot{\xi} > 0 \\ \partial_{\boldsymbol{\sigma}}\phi : \boldsymbol{S}^{-1} : \partial_{\boldsymbol{\sigma}}\phi + \partial_{\xi}\phi, & \dot{\xi} < 0 \end{cases} \\
&= \begin{cases} -||\partial_{\boldsymbol{\sigma}}\phi||_{\boldsymbol{S}^{-1}}^2 - \rho b^M < 0, & \dot{\xi} > 0 \\ ||\partial_{\boldsymbol{\sigma}}\phi||_{\boldsymbol{S}^{-1}}^2 - \rho b^M > 0, & \dot{\xi} < 0 \end{cases}
\end{aligned}
\tag{3.31}
$$

Equation 3.31 states that $\phi(\boldsymbol{\sigma}, \xi)$ versus ξ monotonically decreases with a negative slope by increasing ξ in case of forward transformation. Moreover, the function ϕ is convex for forward transformation as shown in Figure 3.1. These characteristics make the transformation correction well suited for a solution by Newton's method, which is used in this work. Similarly, Equation 3.31 implies that $\phi(\boldsymbol{\sigma}, \xi)$ monotonically decreases with decreasing ξ with a positive slope for reverse transformation. However, the function ϕ is concave for reverse transformation as shown in Figure 3.2. These two observations imply that the application of Newton's method for the transformation correction will only be locally convergent. Attention is now focused on the application of the return mapping algorithm on the discretized SMA constitutive model based on the backward Euler and forward Euler integration methods. Again consider the time interval $[0,t]$ and assume that at the starting time instant $t_n \in [0, t]$, $\boldsymbol{\varepsilon}$, T, and the internal state variables, $\boldsymbol{\varepsilon}^t$ and ξ, are known a priori, i.e.

$$
\boldsymbol{\varepsilon}|_{t=t_n} = \boldsymbol{\varepsilon}_n, T|_{t=t_n} = T_n, \boldsymbol{\varepsilon}^t|_{t=t_n} = \boldsymbol{\varepsilon}_n^t, \xi|_{t=t_n} = \xi_n
\tag{3.32}
$$
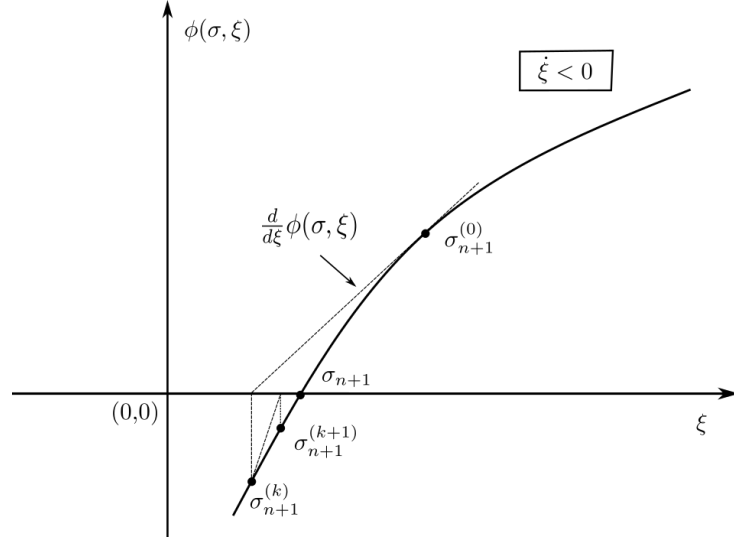
Figure 3.1: Forward transformation: yield function ϕ monotonically decreases with increasing ξ with a negative slope[1]
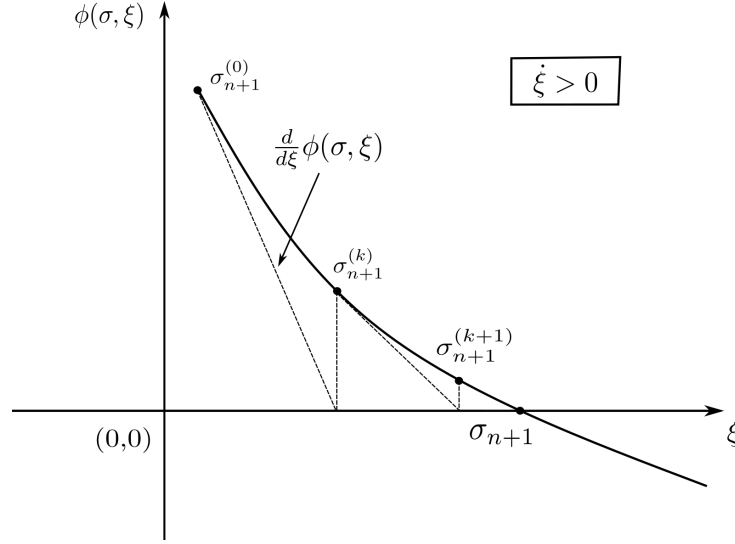
Figure 3.2: Backward Transformation: Yield function ϕ monotonically decreasing with decreasing ξ with a positive slope [1]

3.2.2 Convex Cutting Plane Return Mapping Algorithm

Convex cutting plane return mapping algorithm is formulated on the basis of the transformation function, the consistency condition, direction of the transformation flow and the elastic stiffness tensors without evaluating any gradient. The basic idea relies on integrating the transformation correction equations in, an explicit manner and linearizing the consistency condition. The Newton iteration method is only applied to calculate the increment of martensitic volume fraction, $\Delta\xi_{n+1}^{(k)}$. This enables the convergence of the algorithm towards the final value of the state variables at a quadratic rate; but, convergence is not guaranteed. Here we assume transformation loading; that is, the thermoelastic prediction does not satisfy the transformation condition and $\phi_{n+1}^{(0)} > 0$. Recalling that the total strain tensor, $\boldsymbol{\varepsilon}$, and temperature, T , are fixed, the transformation flow rule given by equation

3.2.2.1 Thermoelastic Prediction

$$
\begin{aligned}
\boldsymbol{\varepsilon}_{n+1} &= \boldsymbol{\varepsilon}_n + \Delta\boldsymbol{\varepsilon}_{n+1} \\
T_{n+1} &= T_n + \Delta T_{n+1} \\
\boldsymbol{\varepsilon}_{n+1}^{t}{}^{(0)} &= \boldsymbol{\varepsilon}_n^{t} \\
\xi_{n+1}^{(0)} &= \xi_n
\end{aligned}
\tag{3.33}
$$

where, $\{\Delta T_{n+1},\ \Delta\boldsymbol{\varepsilon}_{n+1}\}$ are the specified increment in temperature and strain tensor respectively, over the time step $[t_n, t_{n+1}]$, and $(*)^{(0)}$ signifies the values obtained in the prediction stage. An operator split technique is used for the computational implementation by introducing the following trial thermoelastic state:

$$
\begin{aligned}
\boldsymbol{\sigma}_{n+1}{}^{(0)} &:= \boldsymbol{S}_n^{-1} : [\boldsymbol{\varepsilon}_{n+1} - \boldsymbol{\alpha}_n(T_{n+1} - T_0) - \boldsymbol{\varepsilon}_n^{t}] \\
\phi_{n+1}{}^{(0)} &:= \phi[\boldsymbol{\sigma}_{n+1}^{(0)}, T_{n+1}, \xi_n]
\end{aligned}
\tag{3.34}
$$

43

The material properties $\boldsymbol{S}$ and $\boldsymbol{\alpha}$ depend on ξ_n. Note that this problem is solved using the converged internal state variable of the previous time step and the increment of total strain tensor. Physically the reformulation means that this trial state is obtained by neglecting the transformation during the time step, i.e. $\xi_n = 0$. At this stage, if the transformation criterion is $\phi(\boldsymbol{\sigma}_{n+1}^{(0)}, T_{n+1}, \xi_n) \leq 0$ then this trial thermoelastic state is the final state. If, $\phi(\boldsymbol{\sigma}_{n+1}^{(0)}, T_{n+1}, \xi_n) > 0$ then the Kuhn-Tucker conditions are violated and the trial state lies outside the transformation surface. Transformation correction employing backward Euler integration of the flow rule then used to restore consistency and the solution $[\boldsymbol{\sigma}_{n+1}^{(0)}, T_{n+1}, \xi_n]$ is taken as the initial condition for the transformation corrector phase.

3.2.2.2 Transformation Correction

$$\Delta\boldsymbol{\varepsilon}_{n+1}^{t(k)} = \Delta\xi_{n+1}^{(k)}\boldsymbol{\Lambda}_{n+1}^{(k)} \tag{3.35}$$

this explicit integration is being carried out from the initial thermoelastic state to the final unknown state. Now using the discretized flow rule,the stress increment for the kth iteration during the $(n+1)^{th}$ increment can be written as

$$\Delta\boldsymbol{\sigma}_{n+1}^{t(k)} = -\boldsymbol{S}_{n+1}^{(k)-1}\Delta\xi_{n+1}^{(k)} \begin{cases} \partial_{\boldsymbol{\sigma}}\phi_{n+1}^k, & \dot{\xi} > 0 \\ -\partial_{\boldsymbol{\sigma}}\phi_{n+1}^k, & \dot{\xi} < 0 \end{cases} \tag{3.36}$$

Linearizing the discrete transformation function for the kth iteration and equating it to zero due to the Kuhn-Tucker condition,

$$\phi_{n+1}^k + \partial_{\boldsymbol{\sigma}}\phi_{n+1}^k : \Delta\boldsymbol{\sigma}_{n+1}^k + \partial_\xi\phi_{n+1}^k\Delta\xi_{n+1}^k = 0 \tag{3.37}$$

Substituting above two equations and solving for the increment in ξ

$$\Delta\xi_{n+1}^{(k)} = \frac{\phi_{n+1}^{(k)}}{\pm\partial_{\boldsymbol{\sigma}}\phi_{n+1}^{(k)} : \mathscr{E}_{n+1}^{(k)} : \partial_{\boldsymbol{\sigma}}\phi_{n+1}^{(k)} - \partial_\xi\phi_{n+1}^{(k)}} \tag{3.38}$$

where, $+$ sign is for forward transformation and $-$ sign is for reverse transformation. And the next step is to update the transformation strain and martensitic volume fraction.

$$\boldsymbol{\varepsilon}_{n+1}^{t(k+1)} = \boldsymbol{\varepsilon}_{n+1}^{t(k)} + \Delta\boldsymbol{\varepsilon}_{n+1}^{t(k)} \tag{3.39}$$

$$\xi_{n+1}^{(k+1)} = \xi_{n+1}^{(k)} + \Delta\xi_{n+1}^{(k)} \tag{3.40}$$

The flowchart given in Figure 3.3 describes the return mapping algorithm.

$$k = 0,\ \xi_{n+1}^{(0)} = \xi_n,\ \boldsymbol{\varepsilon}_{n+1}^{t(0)} = \boldsymbol{\varepsilon}_n^t,\ \mathcal{S}_{n+1}^{(0)} = \mathcal{S}_n,\ \boldsymbol{\alpha}_{n+1}^{(0)} = \boldsymbol{\alpha}_n$$

$$\boldsymbol{\sigma}_{n+1}^{(k)} := \mathcal{S}_{n+1}^{(k)^{-1}} : [\boldsymbol{\varepsilon}_{n+1} - \boldsymbol{\alpha}_{n+1}^{(k)}(T_{n+1} - T_0) - \boldsymbol{\varepsilon}_{n+1}^{t(k)}]$$
$$\phi_{n+1}^{(k)} := \phi[\boldsymbol{\sigma}_{n+1}^{(k)}, T_{n+1}, \xi_{n+1}^{(0)}]$$

$$\left| \phi_{n+1}^{(k)} \right| \leq TOL$$

Yes

No

Update
$$T_{n+1} = T_n + \Delta T$$
$$\varepsilon_{n+1} = \varepsilon_n + \Delta \varepsilon$$

Update
$$\mathcal{S}_{n+1}^{(k)^{-1}},\ \boldsymbol{\alpha}_{n+1}^{(k)},$$
$$k = k + 1$$

$$\Delta \xi_{n+1}^{(k)} = \frac{\phi_{n+1}^{(k)}}{\partial_{\boldsymbol{\sigma}} \phi_{n+1}^{(k)} : \mathcal{S}_{n+1}^{(k)^{-1}} : \partial_{\boldsymbol{\sigma}} \phi_{n+1}^{(k)} - \partial_{\xi} \phi_{n+1}^{(k)}} (\text{Forward})$$
$$\Delta \boldsymbol{\varepsilon}_{n+1}^{t(k)} = \Delta \xi_{n+1}^{(k)} \boldsymbol{\Lambda}_{n+1}^{(k)} (\text{Forward})$$
$$\Delta \xi_{n+1}^{(k)} = \frac{\phi_{n+1}^{(k)}}{-\partial_{\boldsymbol{\sigma}} \phi_{n+1}^{(k)} : \mathcal{S}_{n+1}^{(k)^{-1}} : \partial_{\boldsymbol{\sigma}} \phi_{n+1}^{(k)} - \partial_{\xi} \phi_{n+1}^{(k)}} (\text{Backward})$$
$$\Delta \boldsymbol{\varepsilon}_{n+1}^{t(k)} = \Delta \xi_{n+1}^{(k)} \boldsymbol{\Lambda}_{n+1}^{(k)} (\text{Backward})$$

$$\xi_{n+1}^{(k+1)} = \xi_{n+1}^{(k)} + \Delta \xi_{n+1}^{(k)}$$
$$\boldsymbol{\varepsilon}_{n+1}^{t(k+1)} = \boldsymbol{\varepsilon}_{n+1}^{t(k)} + \Delta \boldsymbol{\varepsilon}_{n+1}^{t(k)}$$

If $\xi \geq 1$?
(Forward)
or
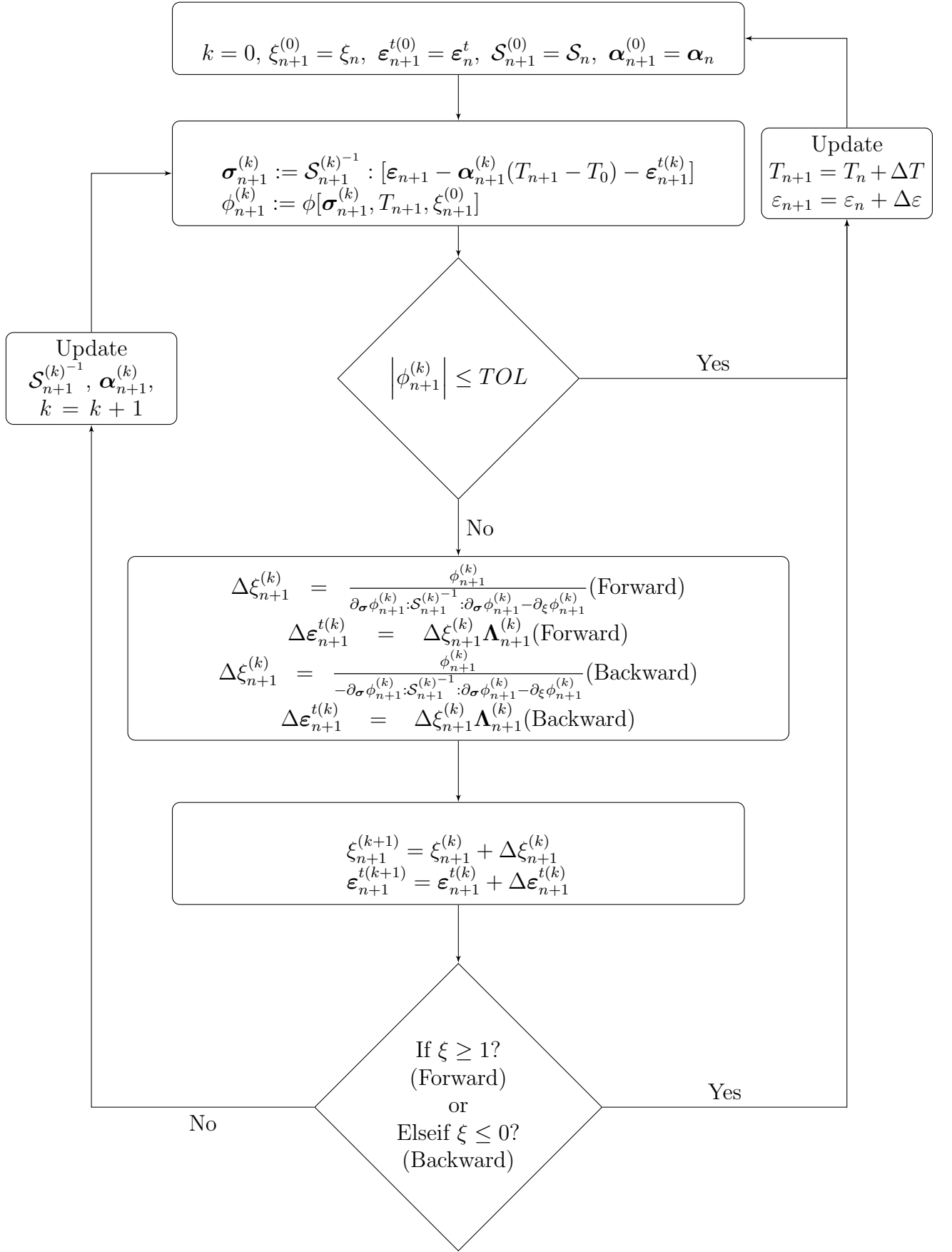Elseif $\xi \leq 0$?
(Backward)

No

Yes

Figure 3.3: Flowchart for Convex Cutting Plane Algorithm

45

3.3   Finite Element Modelling of SMA

In order to develop the finite element model capable of analysing materials with a non-linear constitutive relation, an incremental displacement based formulation is used. The load is increased in a step-by-step pattern. In each loading step, the problem is linearized and an incremental displacement field is found. The final solution in each step can be obtained by superposing the incremental solution with the total solution that is known up to the last load step. The stress equilibrium equation of a generalised of a continuum equation can be written as

$$\boldsymbol{\nabla}.\boldsymbol{\sigma} + \boldsymbol{f}^B = \boldsymbol{0} \qquad (3.41)$$

The incremental displacement field based formulation can be expressed as

$$\boldsymbol{u} = \bar{\boldsymbol{u}} + \Delta\boldsymbol{u} \qquad (3.42)$$

Using the shape functions, the displacement vector can be expressed in terms of nodal variables based on the traditional finite element procedure which leads to

$$\Delta\boldsymbol{u} = [\boldsymbol{\phi}]\{\Delta\boldsymbol{\alpha}\} \qquad (3.43)$$

where, $[\boldsymbol{\phi}]$ represents the shape function and $\Delta\boldsymbol{\alpha}$ denotes the degrees of freedom for the element. Assuming linear displacement relations, the strain and stress fields can be expressed similar to the displacement field as

$$\boldsymbol{\epsilon} = \bar{\boldsymbol{\epsilon}} + \Delta\boldsymbol{\epsilon}$$
$$\boldsymbol{\sigma} = \bar{\boldsymbol{\sigma}} + \Delta\boldsymbol{\sigma} \qquad (3.44)$$

where, $\bar{\boldsymbol{\sigma}}$ and $\bar{\boldsymbol{\epsilon}}$ represent the accumulated stress and strain up to the last step. The quantities $\Delta\boldsymbol{\epsilon}$ and $\Delta\boldsymbol{\sigma}$ stand for the increment of stress and strain in the current step. The incremental strain components $\Delta\boldsymbol{\epsilon}$ associated with the displacement field of equation (Equation 3.42) can be expressed in terms of nodal degrees of freedom as,

$$\Delta\boldsymbol{\epsilon} = [\boldsymbol{B}]\{\Delta\boldsymbol{\alpha}\} \qquad (3.45)$$

In order to derive the element tangent equations, the equilibrium of the body should be expressed using the principle of virtual displacements in the current step. The weak form of the stress equilibrium equation (Equation 3.41) is derived by multiplying a virtual displacement field $\delta\boldsymbol{u}$, integrated over the domain occupied by the solid, and after well-known derivations, they take the form of virtual work equation, which represents the

principle of virtual displacements.

$$\int_V \delta\boldsymbol{\epsilon}^T \boldsymbol{\sigma} dV = \int_V \delta\boldsymbol{u}^T \boldsymbol{f^B} dV + \int_{S_f} \delta\boldsymbol{u}^T \boldsymbol{f^S} dS \tag{3.46}$$

The term in the left-hand side (LHS) of the equation represents the virtual strain energy, the first and second term in the right hand side(RHS) represent the virtual work of body forces ($\boldsymbol{f^B}$) and surface traction forces ($\boldsymbol{f^S}$). Substituting Equation 3.44 in to Equation 3.46 and using incremental Equation 3.18

$$\int_V \delta\boldsymbol{\epsilon}^T \bar{\boldsymbol{\sigma}} \, dV + \int_V \delta\boldsymbol{\epsilon}^T \boldsymbol{L}\Delta\boldsymbol{\epsilon} dV + \int_V \delta\boldsymbol{\epsilon}^T \boldsymbol{\Theta}\Delta T dV = \int_V \delta\boldsymbol{u}^T \boldsymbol{f^B} dV + \int_{S_f} \delta\boldsymbol{u}^T \boldsymbol{f^S} dS \tag{3.47}$$

where $\boldsymbol{L}$ and $\boldsymbol{\Theta}$ are tangent stiffness tensor and tangent thermal moduli tensor respectively. Now, the element tangent equations can be obtained by substituting Equation 3.43 and (3.45) into (3.47), which after rearrangement gives

$$\boldsymbol{K}_T\{\Delta\boldsymbol{\alpha}\} = \boldsymbol{F}^{ext} - \boldsymbol{F}^{int} \tag{3.48}$$

where, $\boldsymbol{K}_T$ corresponds to the tangent stiffness matrix.

$$\boldsymbol{K}_T = \int_V \boldsymbol{B}^T \boldsymbol{L} \boldsymbol{B} dV$$

$$\boldsymbol{F}^{ext} = \int_V [\phi]^T \boldsymbol{f^B} dV + \int_{S_f} [\phi]^T \boldsymbol{f^S} dS$$

$$\boldsymbol{F}^{int} = \int_V \boldsymbol{B}^T (\bar{\boldsymbol{\sigma}} + \boldsymbol{\Theta}\Delta T) dV$$

The nonlinear finite element equation (Equation 3.48) is solved using the iterative Newton-Raphson method. Force is incremented in small steps. At each load step, Newton-Raphson iterative scheme is applied to find the displacement. First, the magnitude of imbalance force is measured, which is the difference of externally applied load ($\boldsymbol{F}^{ext}$) and internally generated stress ($\boldsymbol{F}^{int}$). Then by multiplying the inverse of tangent stiffness matrix ($\boldsymbol{K}_T$) and imbalance force, the increment in displacement is found out. The displacement is updated by adding the increment to the previous one. This process is continued until a convergence criterion is satisfied (Figure 3.4).
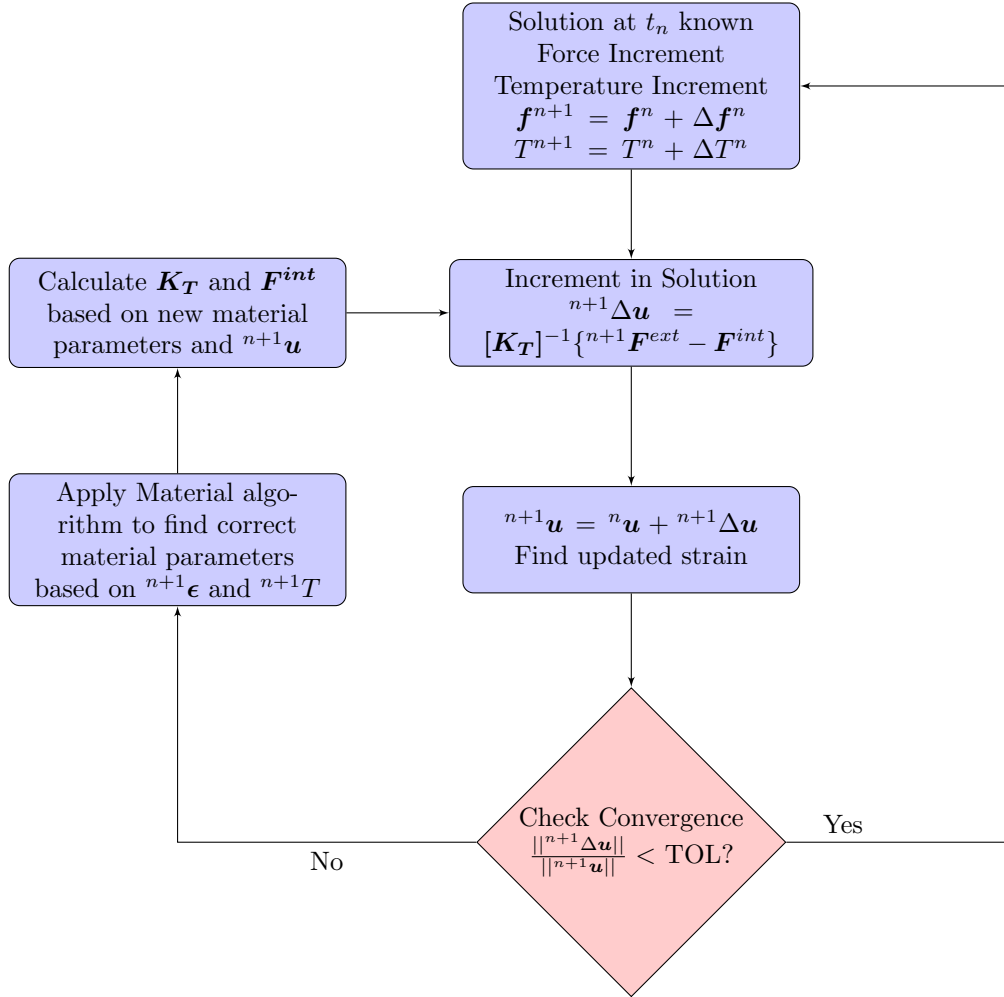
47

Figure 3.4: Flowchart for finite element implementation

3.4 Numerical examples

This section consists of the problems for the components made out of shape memory alloy such as Beam and spring. Problems were solved using FE code and their convergence and validation are studied. In the current study, we mainly focus on the pseudoelastic behaviour of SMA.

3.4.1 SMA Beam

Consider a 3D beam having length 0.1 m, height 0.01 m, and thickness 0.0015 m as shown in Figure 3.5. The beam is constrained at the left face and a transeverse load is acting at the right face which is free to deformed. The beam goes through a gradual loading and unloading and its response at various time steps isrecorded in order to look for its pseudoelastic nature and hysteresis. The SMA properties of the spring is given in Table 3.1.
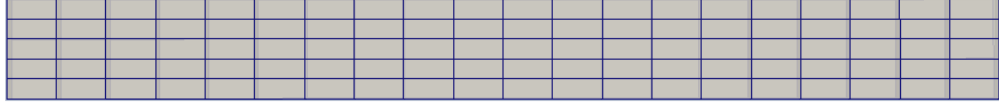

Figure 3.5: Mesh used for FE analysis.

S.No.	Parameter	Value
1	Elastic Modulus of austenite E^A	48.5 GPa
2	Elastic Modulus of martensite, E^M	48.5 GPa
3	Poisson's ratio μ	0.42
4	Coefficient of thermal expansion, α^A	22×10^{-6}
5	Coefficient of thermal expansion, α^M	22×10^{-6}
6	Difference in haet capacity, $c^M - c^A$	0.00
7	Maximum Transformation strain	0.047
8	Austenite finish temperture	315 K
9	Austenite start temperature	295 K
10	Martensite start temperature	291 K
11	Martensite finish temperature	271 K
12	$\rho \Delta c$	0.00

Table 3.1: Material parameters of SMA beam.

Results

The mesh is refined globally till convergence is achieved as shown in Figure 3.6. The convergence occur for 2500 degrees of freedom. The result obtained for SMA beam is again compard with the Elastic counterpart which as shown in Figure 3.7 clearly illustrates the pseudoelastic behaviour of SMA beam and energy dissipated during loading and unloading.
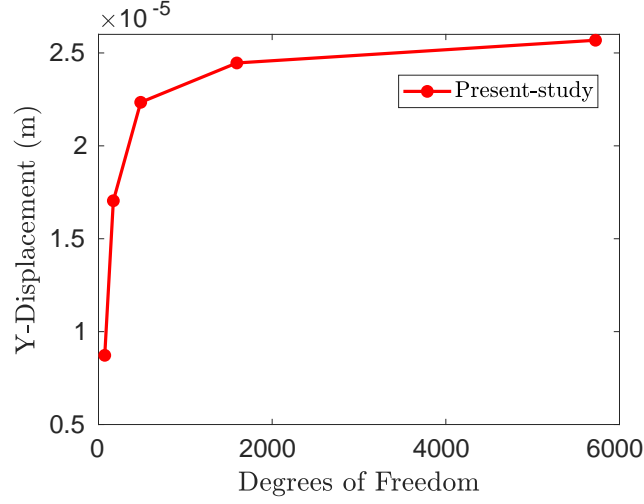

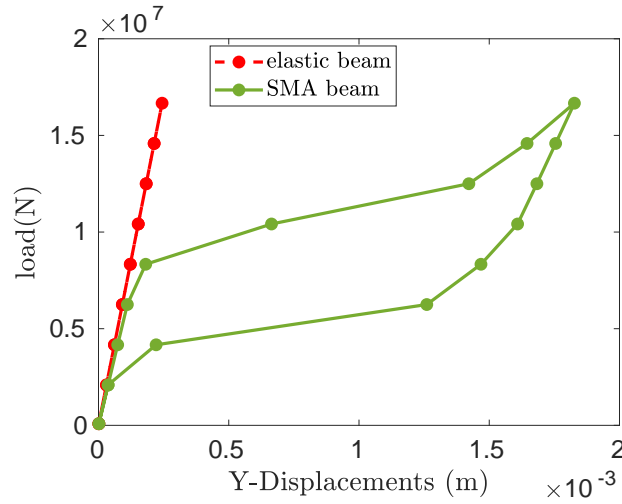Figure 3.6: SMA Beam Convergence study

Figure 3.7: Comparison between elastic and SMA beam behaviour

The solution obtained was validated by the Analytical solution available in the paper

50

"On superelastic bending of shape memory alloy beams" by MeirZafer [28], as well as its martensitic volume fraction change is studied as depicted in Figure 3.8.
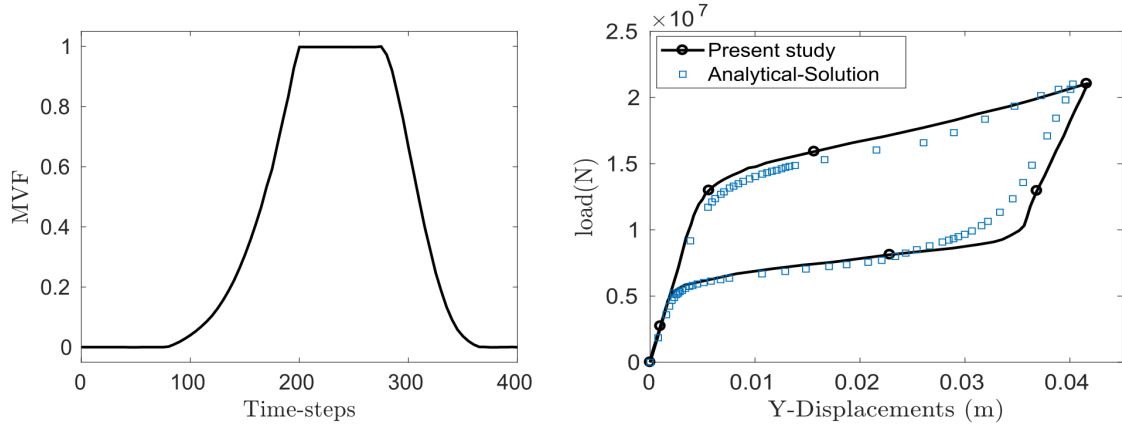

Figure 3.8: (a)Evolution of MVF at fixed end and (b) simulated tip displacement response and validation.

3.4.2 SMA Spring

An SMA helical spring shown in Figure 3.9(a) is used for the analysis. The spring has a mean coil radius of 2.1 cm, an initial length of 12.98 cm and the cross section radius of 6.25 mm. The spring is made from NiTinol Alloy whose material properties are given in table 3.2. The spring is fixed at the lower end, thus any rotation or displacement is zero at lower end and it is loaded at the upper end of the spring. The loading/unloading response of the SMA spring is analyzed by applying the total axial deflection incrementally.
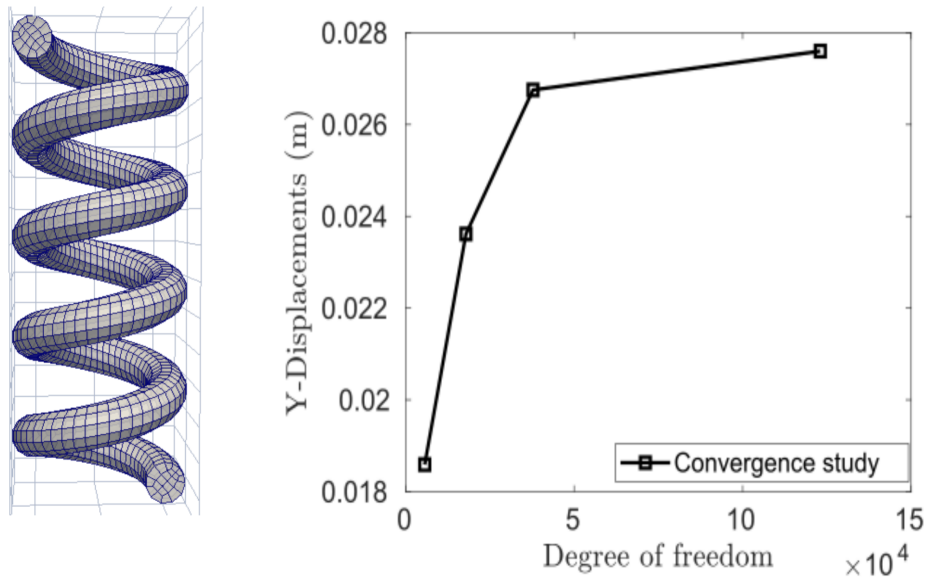

Figure 3.9: (a)Mesh used for analysis and (b) convergence study

S.No.	Parameter	Value
1	Elastic Modulus of austenite E^A	70 GPa
2	Elastic Modulus of martensite, E^M	30 GPa
3	Poisson's ratio μ	0.33
4	Coefficient of thermal expansion, α^A	22×10^{-6}
5	Coefficient of thermal expansion, α^M	22×10^{-6}
6	Difference in haet capacity, $c^M - c^A$	0.00
7	Maximum Transformation strain	0.05
8	Austenite finish temperture	300 K
9	Austenite start temperature	271 K
10	Martensite start temperature	258 K
11	Martensite finish temperature	218 K
12	$\rho\Delta c$	0.00

Table 3.2: Material parameters of SMA helical spring
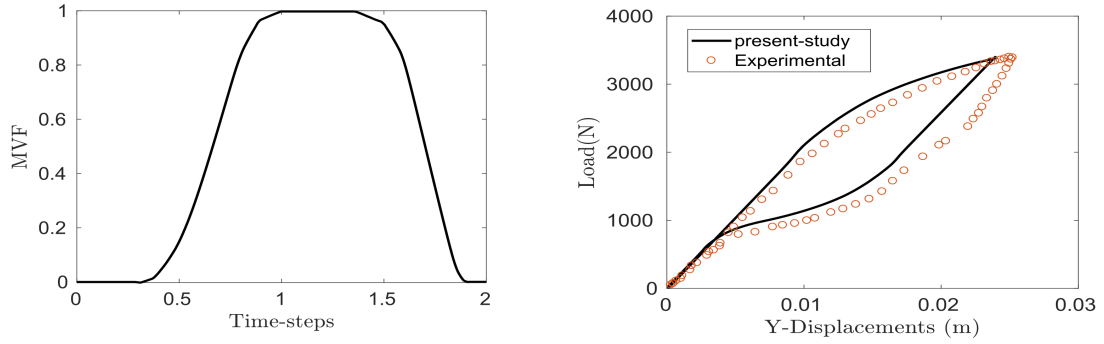
Figure 3.10: (a) Evolution of MVF (b) Simulated tip displacement response and validation.

Results

The convergence study has been shown in Figure 3.9 (b). The spring goes through an loading-unloading cycle. Figure 3.10 illustartes the martensite volume fraction and validation of the analysis. obtained results was validated from the literature "A combined analytical, numerical, and experimental study of shape-memory-alloy helical springs" by Mirzaeifar [29]. As we can see from the MVF-plot, in the first few increments of the laod the entire cross-section remains in the austenite phase only and on further increments, martensitic phase starts to occur.

Chapter 4

Summary and conclusion

In the present work, pseudoelastic response of Shape Memory Alloys (SMA) based members were obtained and convergence and validation study were carried out. The work can be concluded as:

1. Development of FE tool to study the response of elastic structures.

2. Boyd and Lagodous constitutive model [2] was studied and implemented in FE C++ environment using the deal.ii library which is an open-source library to solve partial differential equations using the finite element method.

3. Pseudoelastic response was studied for SMA based members.

4. Different software such as MATLAB and Paraview Client were used for the post-processing analysis. The results obtained for the several elastic and SMA problems were validated through analytical solutions and experimental results available in literature respectively.

4.1   Conclusion

In this report, pseudoelastic behaviour of SMA members such as beam and spring, were studied for a complete loading-unloading cycle. Obtained results efficietnly illustrate the large deformation and phase change that happens in SMA material. It is shown that the analysis done for the SMA beam and spring can predict the martensitic volume fraction and the stress in the material accurately.

4.2   Future Study

Future scope includes study of SMA materials for varying ambient temperature and their effect on the load-displacement response, study of thermomechanical coupling, and large deformation as well as study of use of SMA based members such as SMA spring within

a system, for example in a NonLinear dynamic system [30], in tension-torsion coupling system [31], in morphing wing application [32] to find out their response in varying loading conditions.

Bibliography

[1] D. C. Lagoudas. Shape memory alloys: Modeling and engineering applications, 2008.

[2] James G Boyd and Dimitris C Lagoudas. A thermodynamical constitutive model for shape memory materials. part i. the monolithic shape memory alloy. *International Journal of Plasticity*, 12(6):805–842, 1996.

[3] Jaronie Mohd Jani, Martin Leary, Aleksandar Subic, and Mark A Gibson. A review of shape memory alloy research, applications and opportunities. *Materials & Design (1980-2015)*, 56:1078–1113, 2014.

[4] William J Buehler, John V Gilfrich, and RC Wiley. Effect of low-temperature phase changes on the mechanical properties of alloys near composition tini. *Journal of applied physics*, 34(5):1475–1477, 1963.

[5] Frederick E Wang, William J Buehler, and Stanley J Pickart. Crystal structure and a unique "martensitic" transition of tini. *Journal of Applied Physics*, 36(10):3232–3239, 1965.

[6] Girolamo Costanza and Maria Elisa Tata. Shape memory alloys for aerospace, recent developments, and new applications: A short review. *Materials*, 13(8):1856, 2020.

[7] Jayanth N Kudva. Overview of the darpa smart wing project. *Journal of intelligent material systems and structures*, 15(4):261–267, 2004.

[8] Mohammad Tawfik, Jeng-Jong Ro, and Chuh Mei. Thermal post-buckling and aeroelastic behaviour of shape memory alloy reinforced plates. *Smart Materials and Structures*, 11(2):297, 2002.

[9] Robert G Loewy. Recent developments in smart structures with aeronautical applications. *Smart Materials and Structures*, 6(5):R11, 1997.

[10] Claudio Testa, Stefania Leone, Salvatore Ameduri, et al. Feasibility study on rotorcraft blade morphing in hovering. In *Smart Structures and Materials 2005: Smart Structures and Integrated Systems*, volume 5764, pages 171–182. International Society for Optics and Photonics, 2005.

[11] LG Machado and MA Savi. Medical applications of shape memory alloys. *Brazilian journal of medical and biological research*, 36(6):683–691, 2003.

[12] George F Andreasen and Terry B Hilleman. An evaluation of 55 cobalt substituted nitinol wire for use in orthodontics. *The Journal of the American Dental Association*, 82(6):1373–1375, 1971.

[13] Lorenza Petrini and Francesco Migliavacca. Biomedical applications of shape memory alloys. *Journal of Metallurgy*, 80, 2011.

[14] George B Kauffman and Isaac Mayo. The story of nitinol: the serendipitous discovery of the memory metal and its applications. *The chemical educator*, 2:1–21, 1997.

[15] Jose San Juan. Applications of shape memory alloys to the transport industry. 2006.

[16] Suhas Shreekrishna, Radhika Nachimuthu, and Viswajith S Nair. A review on shape memory alloys and their prominence in automotive technology. *Journal of Intelligent Material Systems and Structures*, 34(5):499–524, 2023.

[17] Alberto Paiva and Marcelo Amorim Savi. An overview of constitutive models for shape memory alloys. *Mathematical problems in engineering*, 2006, 2006.

[18] Kikuaki Tanaka. A thermomechanical sketch of shape memory effect: one-dimensional tensile behavior. *Res. Mechanica*, 18:251–263, 1986.

[19] C. Liang and C.A. Rogers. One-dimensional thermomechanical constitutive relations for shape memory materials. *Journal of Intelligent Material Systems and Structures*, 1:207–234, 1990.

[20] L Catherine Brinson. One-dimensional constitutive behavior of shape memory alloys: thermomechanical derivation with non-constant material functions and redefined martensite internal variable. *Journal of intelligent material systems and structures*, 4(2):229–242, 1993.

[21] A Bekker and L Catherine Brinson. Temperature-induced phase transformation in a shape memory alloy: phase diagram based kinetics approach. *Journal of the Mechanics and Physics of Solids*, 45(6):949–988, 1997.

[22] Dimitris C Lagoudas, Zhonghe Bo, and Muhammad A Qidwai. A unified thermodynamic constitutive model for sma and finite element analysis of active metal matrix composites. *Mechanics of composite materials and structures*, 3(2):153–179, 1996.

[23] Zhonghe Bo and Dimitris C Lagoudas. Thermomechanical modeling of polycrystalline smas under cyclic loading, part iv: modeling of minor hysteresis loops. *International Journal of Engineering Science*, 37(9):1205–1249, 1999.

[24] MA Qidwai and D C Lagoudas. Numerical implementation of a shape memory alloy thermomechanical constitutive model using return mapping algorithms. *International Journal for Numerical Methods in Engineering*, 47(6):1123–1168, 2000.

[25] C Liang and CA Rogers. A multi-dimensional constitutive model for shape memory alloys. *Journal of Engineering Mathematics*, 26(3):429–443, 1992.

[26] Baiyan He, Xuefeng Dong, Rui Nie, Yufeng Wang, Sansan Ao, and Guobiao Wang. Comprehensive shape memory alloys constitutive models for engineering application. *Materials & Design*, 225:111563, 2023. ISSN 0264-1275. doi: https://doi.org/10.1016/j.matdes.2022.111563. URL https://www.sciencedirect.com/science/article/pii/S0264127522011868.

[27] Cheikh Cisse, Wael Zaki, and Tarak Ben Zineb. A review of constitutive models and modeling techniques for shape memory alloys. *International Journal of Plasticity*, 76:244–284, 2016.

[28] Reza Mirzaeifar, Reginald DesRoches, Arash Yavari, and Ken Gall. On superelastic bending of shape memory alloy beams. *International Journal of Solids and Structures*, 50(10):1664–1680, 2013. ISSN 0020-7683. doi: https://doi.org/10.1016/j.ijsolstr.2013.01.035. URL https://www.sciencedirect.com/science/article/pii/S0020768313000504.

[29] Reza Mirzaeifar, Reginald Desroches, and Arash Yavari. A combined analytical, numerical, and experimental study of shape-memory-alloy helical springs. *International Journal of Solids and Structures*, 48:611–624, 02 2011. doi: 10.1016/j.ijsolstr.2010.10.026.

[30] Reza Mehrabi, Mahmoud Kadkhodaei, and Mohammad Elahinia. Constitutive modeling of tension-torsion coupling and tension-compression asymmetry in niti shape memory alloys. *Smart materials and structures*, 23(7):075021, 2014.

[31] Natsuki Tsushima and Masato Tamayama. Recent researches on morphing aircraft technologies in japan and other countries. *Mechanical Engineering Reviews*, 6:19–00197, 07 2019. doi: 10.1299/mer.19-00197.

[32] Julian Colorado, Antonio Barrientos, Claudio Rossi, and Kenny S Breuer. Biomechanics of smart wings in a bat robot: morphing wings using sma actuators. *Bioinspiration & biomimetics*, 7(3):036006, 2012.